



Deep plutonic bodies over low-frequency earthquakes revealed from receiver-side Green's functions

Yasunori Sawaki^{a,b,*}, Yoshihiro Ito^c, Emmanuel Soliman M. Garcia^{c,d}, Ayumu Miyakawa^b, Takuo Shibutani^c

^a Graduate School of Science, Kyoto University, Uji 611-0011, Japan

^b Geological Survey of Japan, National Institute of Advanced Industrial Science and Technology (AIST), Tsukuba 305-8567, Japan

^c Disaster Prevention Research Institute, Kyoto University, Uji 611-0011, Japan

^d National Institute of Physics, University of the Philippines Diliman, Quezon City 1101, Philippines

ARTICLE INFO

Keywords:

Receiver function
Low-velocity zone
Kumano pluton
Slow earthquakes
Fluid process
Nankai Trough

ABSTRACT

Seismological heterogeneity in subduction zones provides insights into slow earthquakes and potential megathrust earthquakes. Studies at the Kii Peninsula in the Nankai subduction zone suggest that there are high-density and high-velocity plutonic bodies in the accretionary prism over the subducting slab, potentially influencing megathrust earthquakes. The lateral variation of heterogeneity and the spatial extent of plutonic bodies remain to be investigated well. Our passive-source imaging of receiver-side Green's functions, from widely distributed campaign seismic observations, reveals a sharp negative S-wave velocity contrast on the top surface of the subducting Philippine Sea plate common to all along-dip profiles and a positive phase tilted upward in the forearc crust. The low permeability of the forearc crust prevents the infiltration of slab-dehydrated fluid further into the upper crust. In the western area, we also found positive phases tilted upward in the forearc crust. The negative phase extends towards the deeper extent of slow-earthquake sources. Meanwhile, the positive phase likely represents the top surface of plutonic rocks of the Kumano and Ohmine plutons that span all the way down to the plate interface. Together with observations of gravity anomaly, intraslab seismicity, and seismic tomography, our interpretation supports the presence of plutonic bodies which extend deep beneath the forearc crust as well as laterally over the subducting PHS slab, rather than a serpentinized mantle wedge. The upper plate is generally low in permeability, but areas with localized high permeability may exist on the updip side of tremor sources. This condition, wherein fluid can infiltrate upwards locally, may maintain the relatively less active slow earthquakes in the western area. The lateral variation of the upper-plate lithology likely influences fluid processes and slow earthquake activities.

1. Introduction

Seismic activity in subduction zones comprises megathrust earthquakes, slab seismicity, and slow earthquakes, which are affected by a variety of factors which include fluid processes and the lithology of the slab as well as upper plate. One of the key aspects is understanding how the abundant fluid in a subducting slab contained within its crust, mantle, and meta-sediment layers influences geophysical phenomena

such as volcanic activity and various modes of seismic slip in the plate subduction system.

Over the past two decades, worldwide geophysical studies have provided a new perspective on the subduction zone system. Slow earthquakes, which have intermediate slip rates between fast earthquakes and fault creep, have now been common phenomena along the subducting plate interface in subduction zones (Ide and Beroza, 2023; Nishikawa et al., 2023; Obara and Kato, 2016; Shelly et al., 2006;

Abbreviations: AIST, National Institute of Advanced Industrial Science and Technology; DPRI, Disaster Prevention Research Institute, Kyoto University, Japan; GF, receiver-side Green's Function; LFE, Low-Frequency Earthquake; Moho, Mohorovičić discontinuity; PHS, Philippine Sea plate; RF, Receiver Function; RJMCMC, Reversible-Jump Markov Chain Monte Carlo; SSE, Slow Slip Event.

* Corresponding author at: Geological Survey of Japan, National Institute of Advanced Industrial Science and Technology (AIST), AIST Tsukuba Central 7, 1-1-1, Higashi, Tsukuba 305-8567, Ibaraki, Japan.

E-mail address: sawaki.yasunori@aist.go.jp (Y. Sawaki).

<https://doi.org/10.1016/j.tecto.2024.230536>

Received 9 April 2024; Received in revised form 30 August 2024; Accepted 13 October 2024

Available online 18 October 2024

0040-1951/© 2024 The Authors. Published by Elsevier B.V. This is an open access article under the CC BY license (<http://creativecommons.org/licenses/by/4.0/>).

Takemura et al., 2023). Slow earthquakes can be detected using seismic and geodetic measurements. Tectonic tremor observed in seismic signals is interpreted as the continuous occurrence of low-frequency earthquakes (LFEs) along the plate interface (Obara, 2002; Shelly et al., 2006, 2007). Geodetically observed slow earthquakes, known as slow slip events (SSEs), frequently coincide with tectonic tremors (Obara et al., 2004; Rogers and Dragert, 2003). Their slip behaviors potentially impact megathrust earthquakes and the surrounding stress states around the plate interface (Ito et al., 2013; Kato et al., 2012; Obara and Kato, 2016).

Seismological heterogeneity around a subduction zone offers a notable perspective for elucidating the source processes of slow earthquakes and potential megathrust earthquakes. The presence of a pronounced low-velocity zone above the subducting slab is a common feature in most of the subduction zones globally (Audet and Kim, 2016). Receiver function (RF) studies have demonstrated a strong negative velocity contrast between the oceanic crust and the overriding forearc plate at the Cascadia (e.g., Abers et al., 2009; Audet et al., 2009), Alaska (e.g., Kim et al., 2014), Mexico (e.g., Pérez-Campos et al., 2008), and Nankai (e.g., Akuhara et al., 2017; Sawaki et al., 2021; Shiomi et al., 2008) subduction zones.

At the Nankai subduction zone in southwestern Japan, one of the areas in which a low-velocity zone has previously been detected is the Kii Peninsula (Fig. 1). Two oceanic plates, the Philippine Sea (PHS) plate and the Pacific plate, are subducting beneath southwestern Japan (Fig. 1b). The PHS plate subducts beneath the Amurian continental plate in a northwest direction, while the Pacific slab subducts deeply beneath the PHS slab toward the west, resulting in deep intraslab earthquakes (Fig. 1a). The subduction of the PHS slab has contributed to huge earthquakes historically and also various types of slow earthquake activities. Deep tectonic tremor occurs at depths of 30–40 km, illuminating a belt-like distribution (Fig. 1b) (Obara, 2002). Kato et al. (2014) conducted tomographic and RF analyses at the western Kii Peninsula and showed possible subsurface structures of the mantle wedge corner and a forearc Mohorovičić discontinuity (Moho) slanted up to the seaward. They implied that LFEs occurred at the serpentinized mantle wedge (Kato et al., 2014).

Tectonic tremor exhibits an along-dip bimodal distribution: updip episodic tremor accompanied by short-term SSEs and downdip continual

tremor (Obara et al., 2010). At the northeastern Kii Peninsula, a previous study found that the RF phase for the top surface of the PHS crust clearly exhibited depth-dependent variation: a sharp and notable negative velocity contrast on episodic tremor sources and a broad and distinctive phase around continual tremor sources (Sawaki et al., 2021). This result provided new insight into the source environment of deep slow earthquakes: the episodic tremor and LFEs can also occur beneath the impermeable forearc crust at the Nankai subduction zone (Sawaki et al., 2021), and not only around the mantle wedge corner (Kato et al., 2010a). The depth-dependent velocity contrast likely reflects the transition in upper-plate permeability and fluid processes (Abers et al., 2013; Audet et al., 2009; Sawaki et al., 2021). Thus, upper-plate lithology can also be a leading factor in illuminating multimodal slip behaviors and fluid processes (e.g., Egbert et al., 2022).

The Kii Peninsula is characterized by an ancient accretionary prism, fundamentally classified as the Shimanto Belt. However, igneous complexes are also exposed on the surface (Fig. 2b). The subduction of the PHS plate, which began approximately 15 Ma, coincides with the movement of the Izu–Bonin–Mariana Trench. This may have led to significant volcanic activities, resulting in the production of extensive amounts of magma (Kimura et al., 2014). Positive Bouguer gravity anomalies suggest the existence of a substantial volume of plutonic rocks within the forearc crust (accretionary prism) at the southern tip of the Kii Peninsula (Honda and Kono, 2005). Those plutonic rocks are partially exposed on the surface around the southern area as the Kumano Igneous Complex (e.g., Kimura et al., 2022) (Fig. 2b) and are often referred to as the *Kumano pluton*. Seismic refraction tomography also revealed the presence of a high-velocity body representing the intruded Kumano pluton (Kodaira et al., 2006). The spatial variation of seismic anisotropy and local stress anomaly also indicates plutonic intrusions at the southern tip of the Kii Peninsula (Saiga et al., 2011; Uchide, 2020; Uchide et al., 2022).

Recent studies on residual free-air gravity anomaly and refraction tomography showed that wider areas of the forearc crust from central to southern Kii Peninsula are characterized by high-density and high P-wave velocity zones, which can be interpreted as the Kumano pluton (Arnulf et al., 2022; Bassett et al., 2022; Bassett and Watts, 2015). The loading of the high-density Kumano pluton on the subducting PHS slab resulted in the bending of the slab around the source area of the 1944

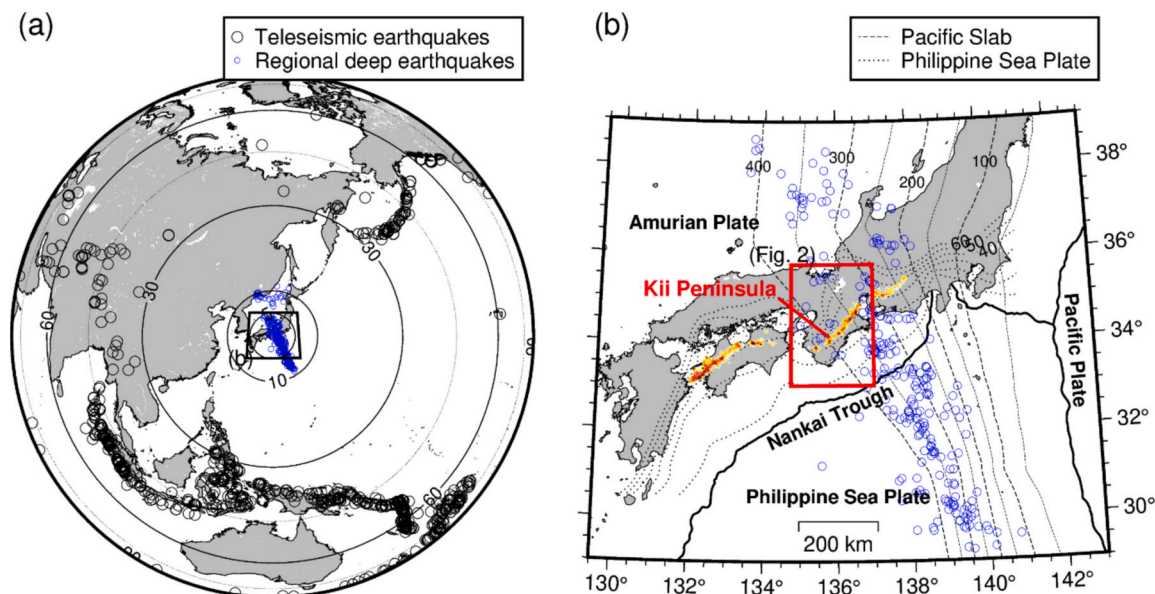


Fig. 1. Target area and seismic events for Green's function (GF) imaging at the Kii Peninsula in southwestern Japan. (a) Black and blue circles are teleseismic and regional deep-focus earthquake events over 200 km depth that occurred in the Pacific slab, respectively. (b) Dashed and dotted lines denote depth contours of the Pacific slab (Nakajima et al., 2009; Nakajima and Hasegawa, 2006) and the Philippine Sea plate, both of which were compiled by Hirose et al. (2008). (For interpretation of the references to colour in this figure legend, the reader is referred to the web version of this article.)

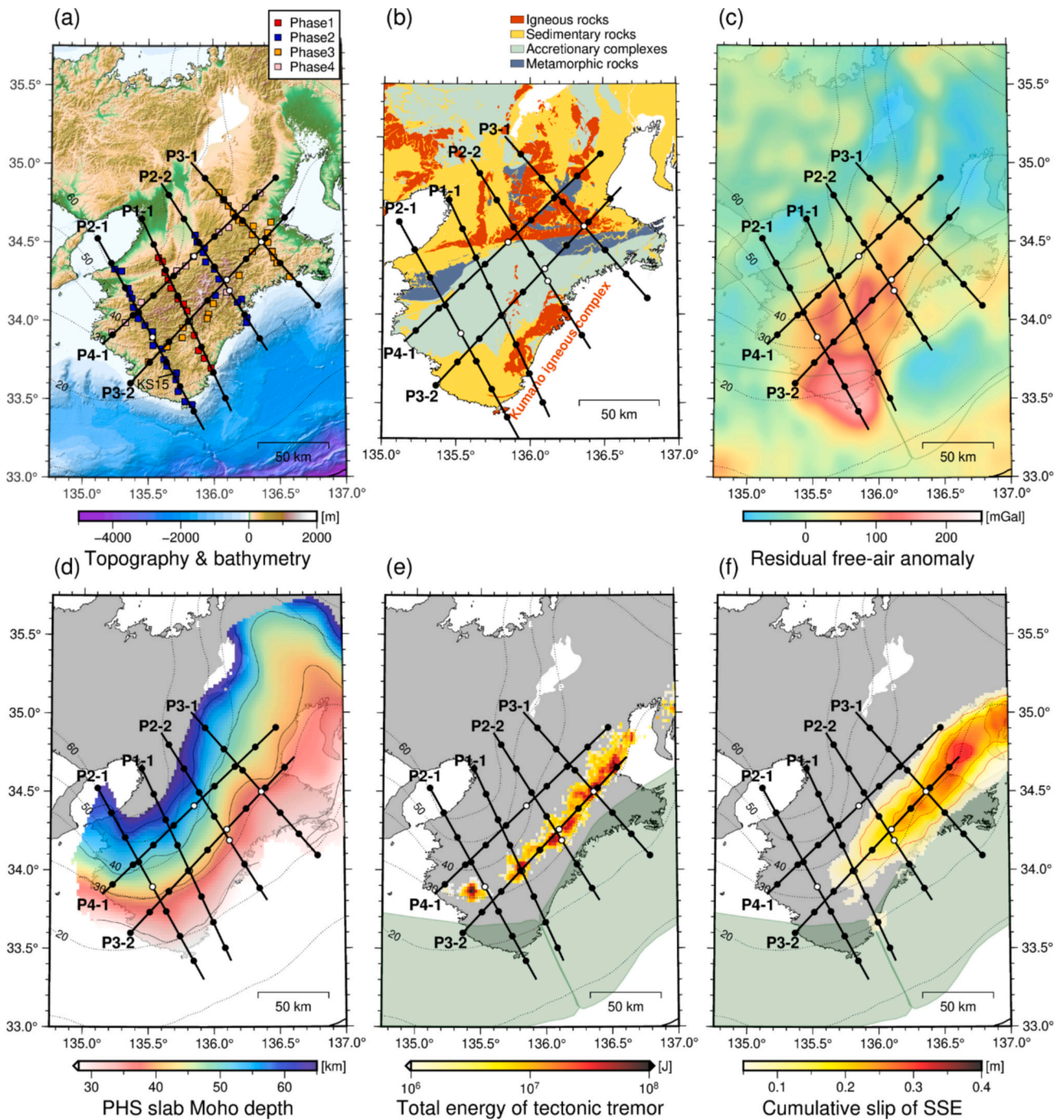


Fig. 2. Tectonic setting and the campaign-type observation. (a) Campaign seismic stations and survey lines for GF imaging at the Kii Peninsula in southwestern Japan. The area depicted is denoted by the red box in Fig. 1b. Dashed lines denote depth contours of the Philippine Sea plate compiled by Hirose et al. (2008). Colors in squares indicate the observation phase. The white circle is the center of each profile and black circles are spaced every 20 km. (b) Geological setting around the Kii Peninsula. The area colored in red represents igneous rocks, and the Kumano igneous complex is exposed at the ground surface around the coast of the southern area. (c) Residual free-air gravity anomaly (Bassett and Watts, 2015). (d) The PHS slab Moho model (Shiomi et al., 2008). Mesh data in (e) and (f) are the total energy of deep tectonic tremor from April 2004 to March 2015 (Annoura et al., 2016) and the cumulative slip of slow slip events from July 1996 to June 2020 (Okada et al., 2022), respectively. The green area indicates the anticipated source regions of megathrust earthquakes. (For interpretation of the references to colour in this figure legend, the reader is referred to the web version of this article.)

Tonankai Earthquake (Arnulf et al., 2022; Bassett et al., 2022). Nakajima (2023) carried out 3-D travel-time tomography analysis and showed an inclined high-velocity anomaly above the PHS slab extending toward the downdip of LFE sources. They also discussed that the rigid and impermeable materials of the Kumano pluton widely overlay the subducting PHS slab and that this leads to a steeper subduction of the slab. However, the spatial extent of the Kumano pluton and its influence

on fluid transport processes related to slow and fast earthquakes have not been well constrained.

Therefore, we investigate the seismological heterogeneity beneath the Kii Peninsula from receiver-side Green's functions (Akuhara et al., 2019). We use and analyze seismic waveforms recorded by campaign-type linear-array observations at the Kii Peninsula, conducted by the Disaster Prevention Research Institute (DPRI) at Kyoto University

(Nishimura et al., 2005; Shibutani and Hirahara, 2017). We provide new seismological insight into the Kumano pluton and structural conditions of slow and fast earthquakes.

2. Data

2.1. Seismic network

DPRI conducted campaign-type linear-array observations in the Kii Peninsula (Nishimura et al., 2005; Shibutani and Hirahara, 2017). Each seismic station was operated for about one half to two years, from 2004 to 2013. We analyzed seismic waveforms recorded at these campaign stations (Fig. 2). We divided observation periods into four phases (Phases 1–4). The survey lines were named P2–1, P1–1, P2–2, and P3–1 from west to east based on the observation phase. Each campaign station is equipped with a short-period (1 s) velocity sensor for three components. We used three-component waveforms, and the radial component was obtained by rotating two horizontal components from the back azimuth of seismic events. Note that the original horizontal components face towards the north and east components as the seismographs were deployed on the surface.

2.2. Seismic events for waveform analysis

We selected teleseismic earthquake events with magnitudes greater than 5.5 and epicentral distances between 30 and 90 degrees (Fig. 1a). After the visual inspection of waveforms, we used 693 events in total. Since the previous study by Sawaki et al. (2021) made use of seismic waveforms generated by regional deep-focus earthquakes that occurred in the Pacific slab, we also used the regional deep-focus earthquakes with a magnitude of greater than 3.5 from the epicentral distance within 10 degrees (Fig. 1a). After the visual selection of waveforms, we chose 329 events in total.

3. Methods

3.1. Receiver-side Green's function

In this study, instead of the conventional RF, we computed receiver-side Green's functions (GFs; Akuhara et al., 2019). Generally, a teleseismic waveform contains information about seismological heterogeneity beneath a receiver. In the conventional method of the P-wave RF, a P-to-S phase in a teleseismic waveform, converted at a S-wave velocity contrast, is extracted from horizontal component waveforms deconvolved by the vertical component (Ammon, 1991). Deconvolution is often performed either in the frequency domain (e.g., Langston, 1979; Shibutani et al., 2008) or in the time domain (e.g., Ligorria and Ammon, 1999; Ökeler, 2021). However, deconvolution in the frequency domain often suffers from computational instability because it involves dividing the vertical-component spectrum which contains spectral holes. The time-domain deconvolution still requires the use of thresholds or controlling algorithms to manage the number of spikes in a resulting RF trace (e.g., Ruan et al., 2023; Wang and Pavlis, 2016). Also, elimination or adjustment of a spike is impossible once it is generated (Kolb and Leki, 2014).

Akuhara et al. (2019) developed a novel method to retrieve seismic responses from S-wave velocity discontinuities, specifically the GF, from teleseismic waveforms by implementing the reversible-jump Markov chain Monte Carlo algorithm (RJCMCMC; Green, 1995). The outcome of the RJCMCMC method is referred to as GF, not RF, because the deconvolution of the vertical component from horizontal components is not performed, meaning that the output is literally the Green's function. The advantage of RJCMCMC is that it can solve the number of model parameters, i.e., the number of spikes in a GF trace, using the transdimensional Bayesian framework. The GF method includes proposals of adding a new spike (birth), deleting an existing spike (death), moving

the time arrival of an existing spike (move), and perturbing a spike amplitude (perturb). A proposal selected from among birth, death, move or perturb ones is either accepted or rejected in each iteration, which achieves the transdimensional Bayesian inference of GF (Akuhara et al., 2019).

We employed their method and computed radial-component GFs. Using the implemented parallel tempering algorithm, we performed 1,000,000 iterations using 10 chains, two of which were at the coolest temperature ($T = 1$; see Akuhara et al., 2019), and sampling models every 200 iterations. Samples from the first 200,000 iterations were discarded to avoid the burn-in period. Since the resulting GF is given as the posterior probability distribution of amplitude, we extracted the model trace of expected values.

The GF method has proven successful for both offshore (e.g., Akuhara et al., 2020, 2023) and onshore data (Leah et al., 2022). Akuhara et al. (2020) computed GF traces from teleseismic waveforms of ocean-bottom seismographs deployed off Kii Peninsula and found a notable low-velocity zone in the upper underthrust sediment that has shallow slow earthquakes. Leah et al. (2022) performed the GF imaging at the northern Hikurangi subduction zone using inland seismic stations and estimated the slab geometry. We will compare the conventional RF and GF in the Results section (Figs. 3 and 4).

3.2. Preprocessing

We estimated the arrival time of the first P-waves using the TauP program (Crotwell et al., 1999). Event waveforms were band-passed between 0.1 and 12.5 Hz, deconvolved by instrumental responses, and cut 5 s before the estimated P arrival. When computing the GF, we applied a Gaussian low-pass filter of 1.9 Hz at -3 dB, which are given by the Gaussian parameter of 10.0.

3.3. Green's function imaging: common-conversion-point stacking

To highlight the lateral variations in crustal structures, we performed common-conversion-point stacking of radial GF traces, a technique often used in RF imaging (Dueker and Sheehan, 1997). We extracted 1-D velocity profiles varying only with depth beneath seismic stations from the 3-D velocity model ALJ2023 (Matsubara et al., 2022) to convert Ps time to depth and to perform the ray tracing. A 2-D transect was meshed into a grid with a spacing of 0.5 km for both the length and depth. $H[l, m]$ represents the stacked GF amplitude for the grid point at $[l, m]$. We selected the stations located within 10 km of the profile line. The GF amplitude at each timing was then projected into a pixel along the ray path. If the distance from the profile line to a pixel d is more than 5 km, the amplitude decays proportionally to the square root of the scaled distance. We also used second-root stacking to enhance coherent signals of the GF amplitude (e.g., Kanasewich et al., 1973; Muirhead, 1968). If N_{lm} rays of GF $g_i^{lm}(t)$ ($i = 1, \dots, N_{lm}$) propagate through the pixel at $t = t_i$, the second-root of the amplitude with its preserved polarity is stacked as follows:

$$\gamma_{lm} = \frac{1}{\sum_{i=1}^{N_{lm}} \max\left(\frac{d_i}{5}, 1\right)^{\frac{1}{2}}} \left| \sum_{i=1}^{N_{lm}} g_i^{lm}(t_i) \max\left(\frac{d_i}{5}, 1\right)^{\frac{1}{2}} \operatorname{sgn}\{g_i^{lm}(t_i)\} \right|. \quad (1)$$

Using γ_{lm} , the stacked amplitude in the grid $[l, m]$ can be represented as

$$H[l, m] = |\gamma_{lm}| \gamma_{lm} \quad (2)$$

If $N_{lm} < 3$, the amplitude value is ignored. After stacking for all the grids, the amplitude was smoothed using a 2-D Gaussian filter.

To reduce the impact of outliers, we estimated the median and median absolute deviation (MAD) amplitudes for each grid from 200 bootstrap samples of GF traces for each profile line. After performing

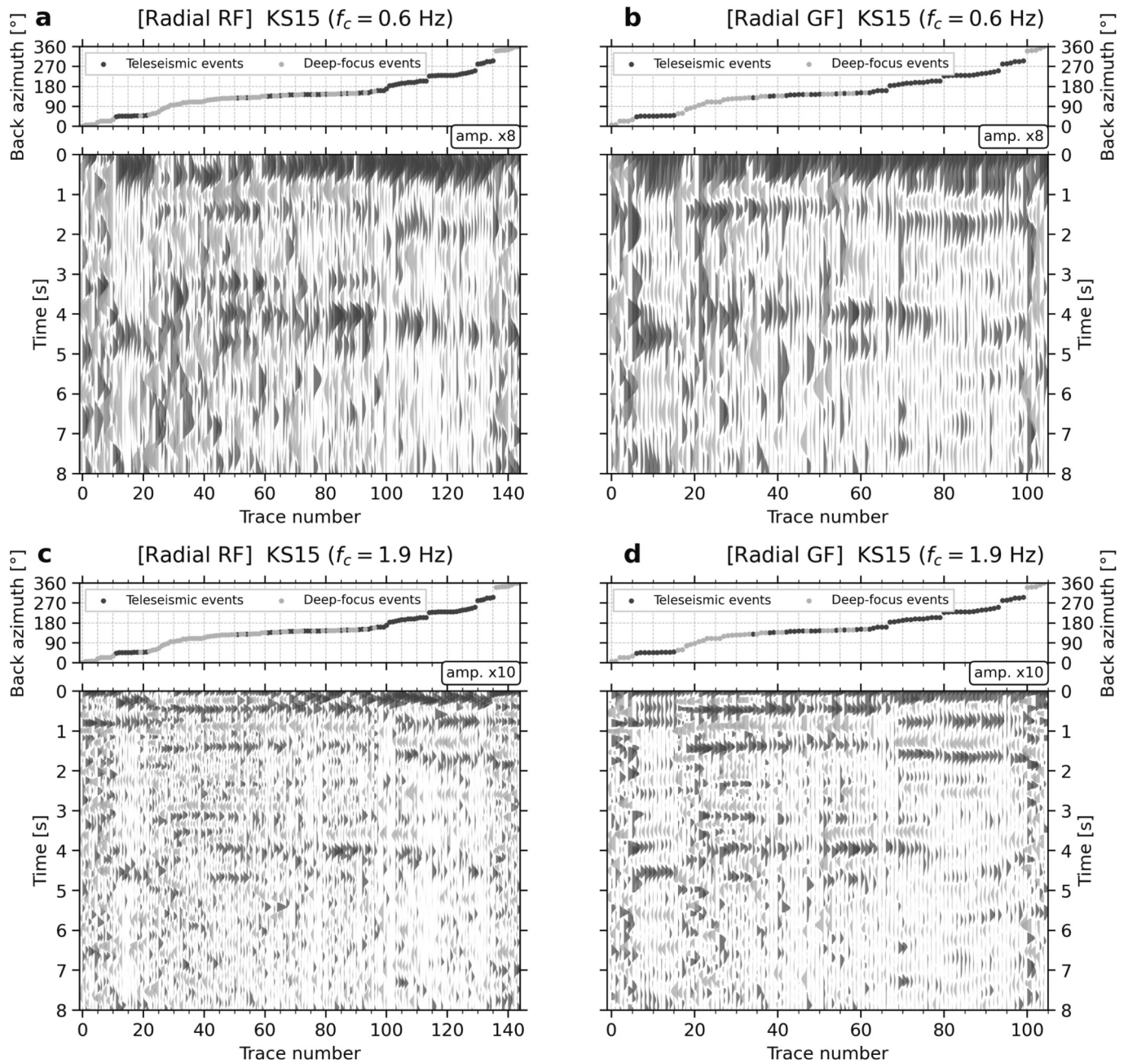


Fig. 3. Example of computed (a,c) receiver function (RF) and (b,d) GF traces at the KS15 station shown in Fig. 2a. Each RF and GF trace is vertically aligned and sorted by the back azimuth shown in the top panels. The areas painted in dark and light gray correspond to the positive and negative amplitudes, respectively. Each trace is amplified by a factor within the white box. Markers in dark and light gray in the top panels represent teleseismic and regional deep-focus earthquake events, respectively. The Gaussian low-pass frequencies at -3 dB are (a,b) ~ 0.6 Hz and (c,d) ~ 1.9 Hz, respectively.

second-root stacking for each bootstrap sample, we obtained the median-amplitude image. Any grid with MAD larger than 0.02 was removed.

4. Results

We begin by presenting a set of RF and GF traces (Fig. 3). These RF traces were computed using the iterative time-domain deconvolution method, as improved by Ruan et al. (2023). Assuming that radial RF and GF phases are attributed to Ps phases from significant velocity contrasts, the positive and negative phases correspond to the top of high- and low-velocity materials, respectively, although those phases can include multiple reverberations from shallow interfaces such as PpPs. For low-

frequency traces (< 0.6 Hz), the phase features of RF and GF are nearly identical, with positive phases around 4 s representing the slab Moho. For broader-band traces (< 1.9 Hz), detected phases are almost the same, but GF traces show sharp and clear phases compared to RF traces. Arrival times of those phases are more consistent among surrounding traces, suggesting that GF suffers less from high-frequency noise or computational instability.

Having confirmed that GF traces can more efficiently retrieve subsurface responses, we performed GF imaging for the survey lines in Fig. 2. Our GF images show clear structures of the upper plate and the subducting PHS slab (Figs. 4–8, S1–S2). GF images are also overlaid with the plate interface model (Hirose et al., 2008) and the oceanic Moho model (Shiomi et al., 2008).

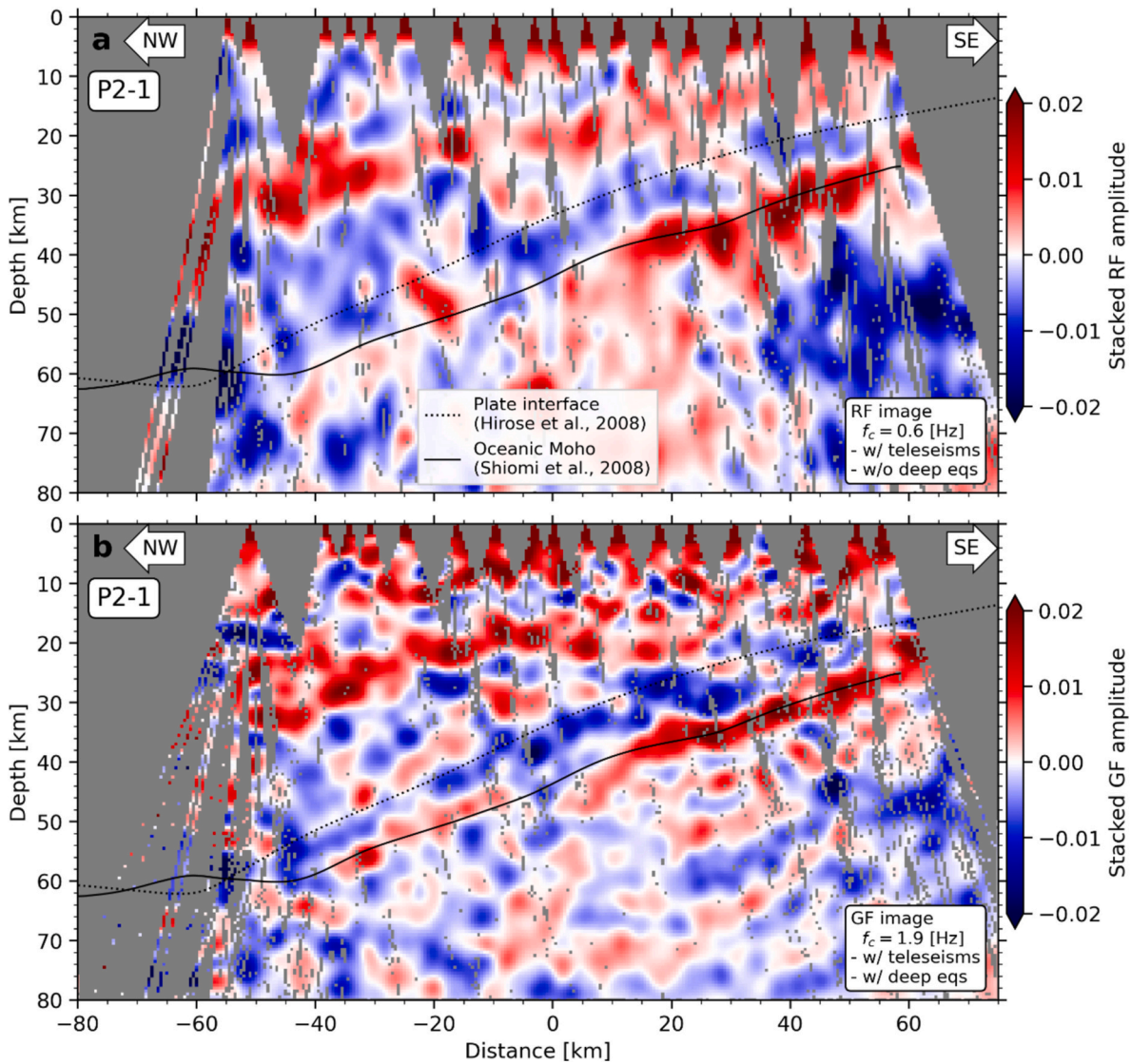


Fig. 4. (a) Conventional RF image and (b) GF image along the cross-sectional profile P2-1 (westernmost profile). Solid and dotted lines show the Philippine Sea plate models of the slab Moho (Shiomi et al., 2008) and the top of the slab (Hirose et al., 2008), respectively.

4.1. Western area (P2-1 and P1-1)

To observe the difference in the frequency range for RF and GF images, we compared the images of conventional low-frequency RFs and broader-band GFs along the P2-1 line (Fig. 4). Several significant phases are observed in both images. At a horizontal position of >15 (km), a positive phase at depths 25–40 km is observed to dip in the northwest direction. This phase is well represented in the depth section of the slab Moho by Shiomi et al. (2008). However, the phase does not appear in the deeper portion of the slab. Previous studies also implied a decrease in the phase-amplitude for the slab Moho (Shiomi et al., 2008; Yamauchi et al., 2003).

Above the positive phase of the slab Moho, we also observed a negative phase that was significant only in the broader-band image. This phase is explained by the depth section of the top of the slab (Hirose et al., 2008). Negative velocity contrasts have been widely reported in various subduction zones (Audet et al., 2009; Sawaki et al., 2021). As we previously demonstrated, the broader-band RF can image the top of a subducting slab more clearly than the low-frequency RF (Sawaki et al., 2021). This result indicates that the velocity change around the plate interface occurs within a narrow zone.

Around the horizontal position of > -55 (km), we observed a

positive phase at approximately 30 km depth tilting toward the south-east direction. Previous studies have interpreted the positive phase as the forearc Moho (Kato et al., 2014; Shibutani et al., 2009). The positive phase is sharper in the broader-band image in the horizontal range of -55 to 0 (km).

We also compared a P-wave velocity model (Arnulf et al., 2022) with our broader-band GF image along the P2-1 line (Fig. 5). The notable feature is the large volume of a high-velocity anomaly in the overriding forearc crust. The positive phase, which is located around a depth of 20 km and spans from -20 km to 40 km along the horizontal in the forearc crust, is situated on or just above the high-velocity anomaly. Nakajima (2023) also showed the broad distribution of the high-rigidity and high-velocity materials in the forearc crust around the western Kii Peninsula. It should be noted that the velocity model from Arnulf et al. (2022) is not well resolved at depths greater than 30 km for lateral positions around <0 (km); we neither observed any positive phase that corresponds to the strong velocity gradient assumed as the forearc Moho in the model from Arnulf et al. (2022). However, we observed the sharp negative phase of the slab top around the horizontal position of > -20 km, which is just beneath the high-velocity materials.

Udpip seismicity around the slab is located on the positive phase for the slab Moho (Fig. 5). As mentioned above, we did not observe a clear

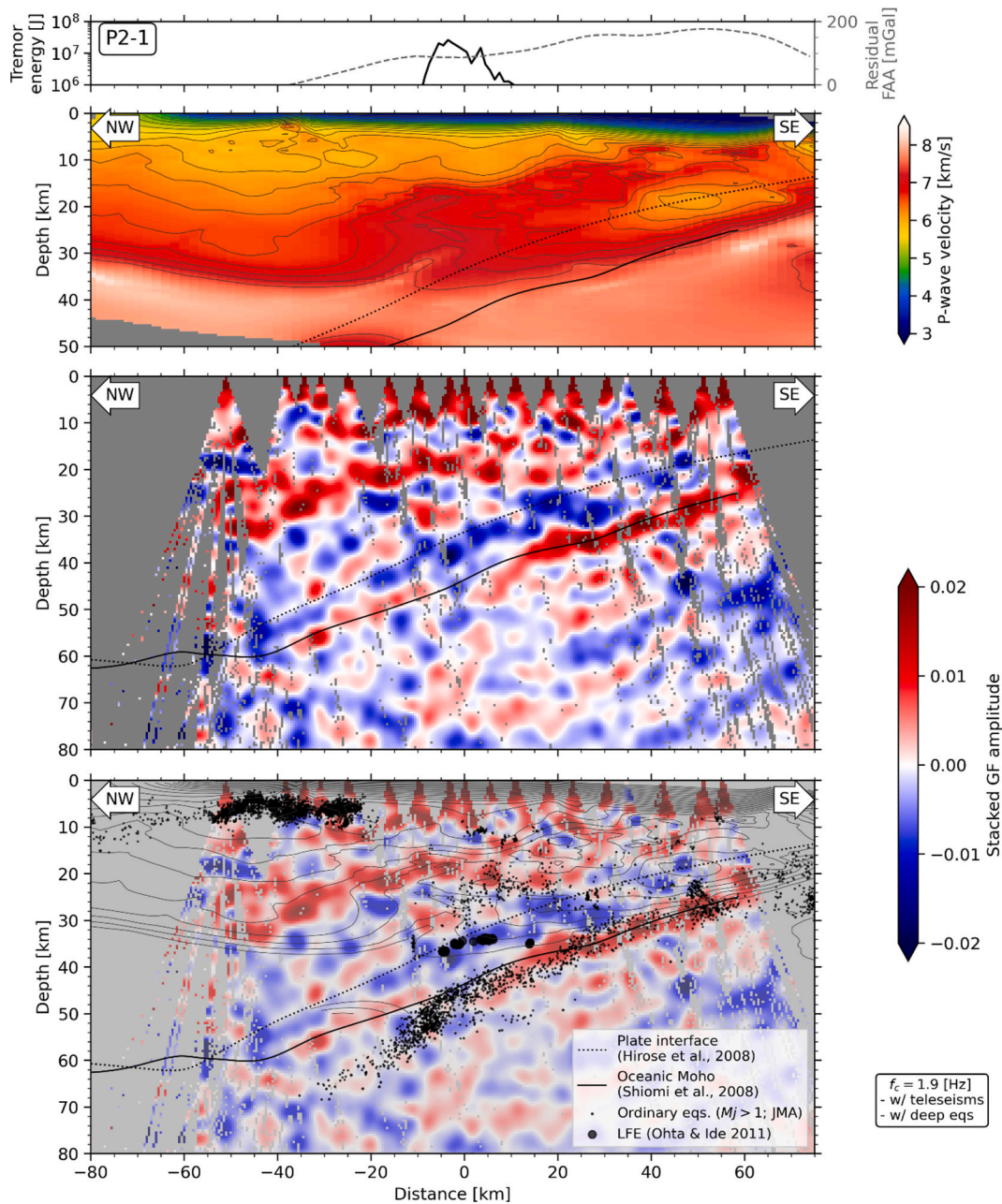


Fig. 5. GF image and P-wave velocity model (Arnulf et al., 2022) in the along-dip profile P2-1 (most western profile). Solid and dashed lines on the top panel are the total energy of tectonic tremor (Annoura et al., 2016) and the residual free-air gravity anomaly (Bassett and Watts, 2015), respectively. The free-air anomaly is averaged over 10 km perpendicular to the survey line. The second panel from the top shows the P-wave velocity structure (Arnulf et al., 2022). Solid and dotted lines show the Philippine Sea plate models of the slab Moho (Shiomi et al., 2008) and the top of the slab (Hirose et al., 2008), respectively. The top of the slab shows our GF image. The bottom panel includes seismic events. Small black dots are the ordinary earthquakes ($M_j \geq 1.0$) in the Japan Meteorological Agency (JMA) unified earthquake catalog from January 2003 to December 2022. The gray solid circles denote the source location of deep low-frequency earthquakes in 2002–2008 (Ohta and Ide, 2011). All plotted events are located within 10 km of the survey line.

slab Moho phase in the downdip portion. The downdip seismicity is also located around 10 km below the negative slab-surface phase without inter-plate earthquakes. Although the hypocenters were not relocated, it is evident that the slab seismicity mostly accounts for the intra-slab seismicity around the top of the slab mantle, not in the oceanic crust (Abers et al., 2013).

Low-frequency earthquakes (LFEs) are situated on the negative slab-top phase (Ohta and Ide, 2011). The cumulative seismic energy of tectonic tremor, which is higher than 10^6 J, accumulates at the lateral position around -10 – 10 km. Given that deep tectonic tremor is a successive occurrence of minor LFE events on the plate interface (Shelly

et al., 2006, 2007), it is likely that tectonic tremor occurs as well on the plate interface that has a clear negative phase.

In the broader-band GF image along the P1-1 line, a clear negative phase for the plate interface exists at the lateral position around -10 – 40 km, and LFEs are located almost on the negative phase (Fig. 6). The slab Moho with positive amplitudes was found at the position between -10 – 40 km, although amplitudes decrease as the slab deepens. The positive phase for the slab Moho is not clear around where numerous intra-slab earthquakes are located. We also observed positive phases at the depth of 20–30 km in the forearc crust at the position between -50 – 30 (km) on or beneath where a high-velocity zone exists (Arnulf

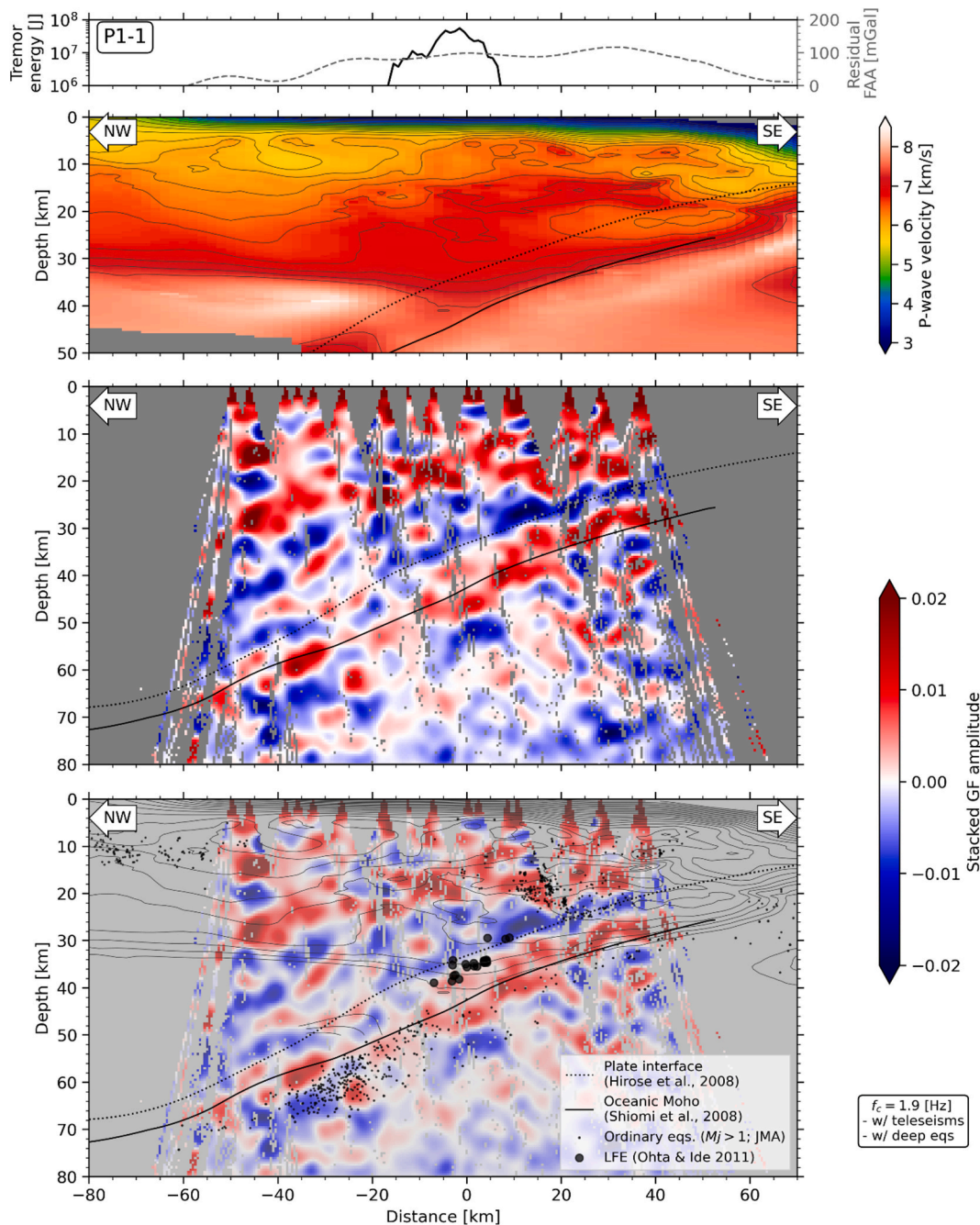


Fig. 6. GF image and P-wave velocity model (Arnulf et al., 2022) in the along-dip profile P1-1. All other details are the same as in Fig. 5.

et al., 2022). The positive phase tilted upward is consistent with previous RF studies (Shibutani et al., 2009; Shiomi et al., 2008; Ueno et al., 2008).

4.2. Central area (P2-2)

The broader-band GF image along the P2-2 line exhibits a clear and sharp negative phase for the plate interface at the horizontal position between -20 – 10 km (Fig. 7). LFEs and tectonic tremor are located almost on the negative phase. The slab Moho with positive amplitudes was found at the position between 10 and 35 km. We were unable to identify a significant positive phase for the slab Moho in the downdip portion.

Similar to the results at the western survey lines (P2-1 and P1-1), we also observed positive phases tilted upward in the forearc crust at the

lateral location along -65 – 10 km. Compared with the P-wave velocity model (Arnulf et al., 2022), however, those positive phases do not correspond to the top of significant high-velocity zones. Instead, the high-velocity zone exists at the position around >0 km, and we observed noisy positive phases that penetrate the high-velocity zone.

4.3. Eastern area (P3-1)

The broader-band GF image along the P3-1 line displays a sharp negative phase for the plate interface at the horizontal position between -5 – 25 km (Fig. 8). LFEs are located almost on the negative phase. The cumulative energy of tectonic tremor exhibits a bimodal distribution (Obara et al., 2010), and downdip tremor is spatially isolated from LFE events. Around the downdip end of tremor source area at 35 km depth, the negative phase for the plate interface becomes broad between -40

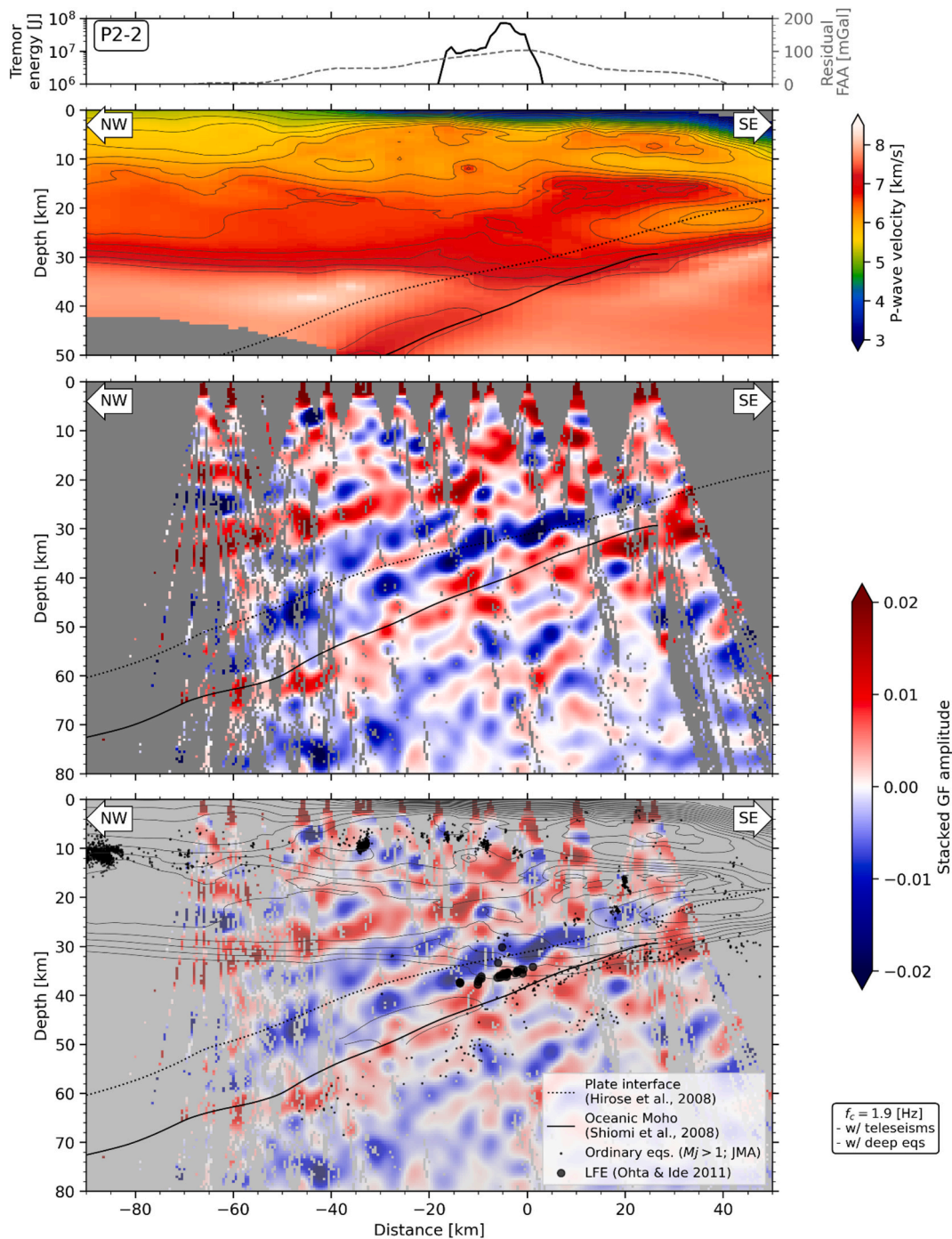


Fig. 7. GF image and P-wave velocity model (Arnulf et al., 2022) in the along-dip profile P2-2. All other details are the same as in Fig. 5.

and 0 km along the horizontal. We observed a broad expansion of negative phases as the slab deepens from the downdip tremor area. Unlike the other along-dip profiles, the slab Moho with positive amplitudes was found all throughout the position between -50 – 30 km. Additionally, the positive phases in the forearc crust are nearly flat at the position between -50 – 10 km, but they suddenly rise upward around -10 – 25 km. These results suggest that the broad negative phases sandwiched by the two positive phases represent the presence of the mantle wedge (Sawaki et al., 2021). While the negative phase for the slab surface does not exhibit a strong amplitude around LFE sources in the P3-1 line compared to that along the updip portion of plate interface, the presence of the continuously narrow phase around LFE sources does not necessarily contradict the undrained condition for the

impermeable crustal seal. This is because a thickened negative phase would appear under a permeable condition such as a serpentinized mantle wedge corner (Sawaki et al., 2021).

4.4. Along-strike profiles (P3-2, P4-1)

We present along-strike images along the P3-2 (Fig. S1) and the P4-1 lines (Fig. S2). Note that those profiles are sub-perpendicular to the direction of the slab dip, so GF phases are rather noisy compared to the along-dip profiles. For the seaward profile P3-2 (Fig. S1), strong negative phases are observed at a depth of 25 – 30 km, but they are several kilometers above the plate interface model (Hirose et al., 2008). Positive phases for the slab Moho are slightly imaged. For the landward profile

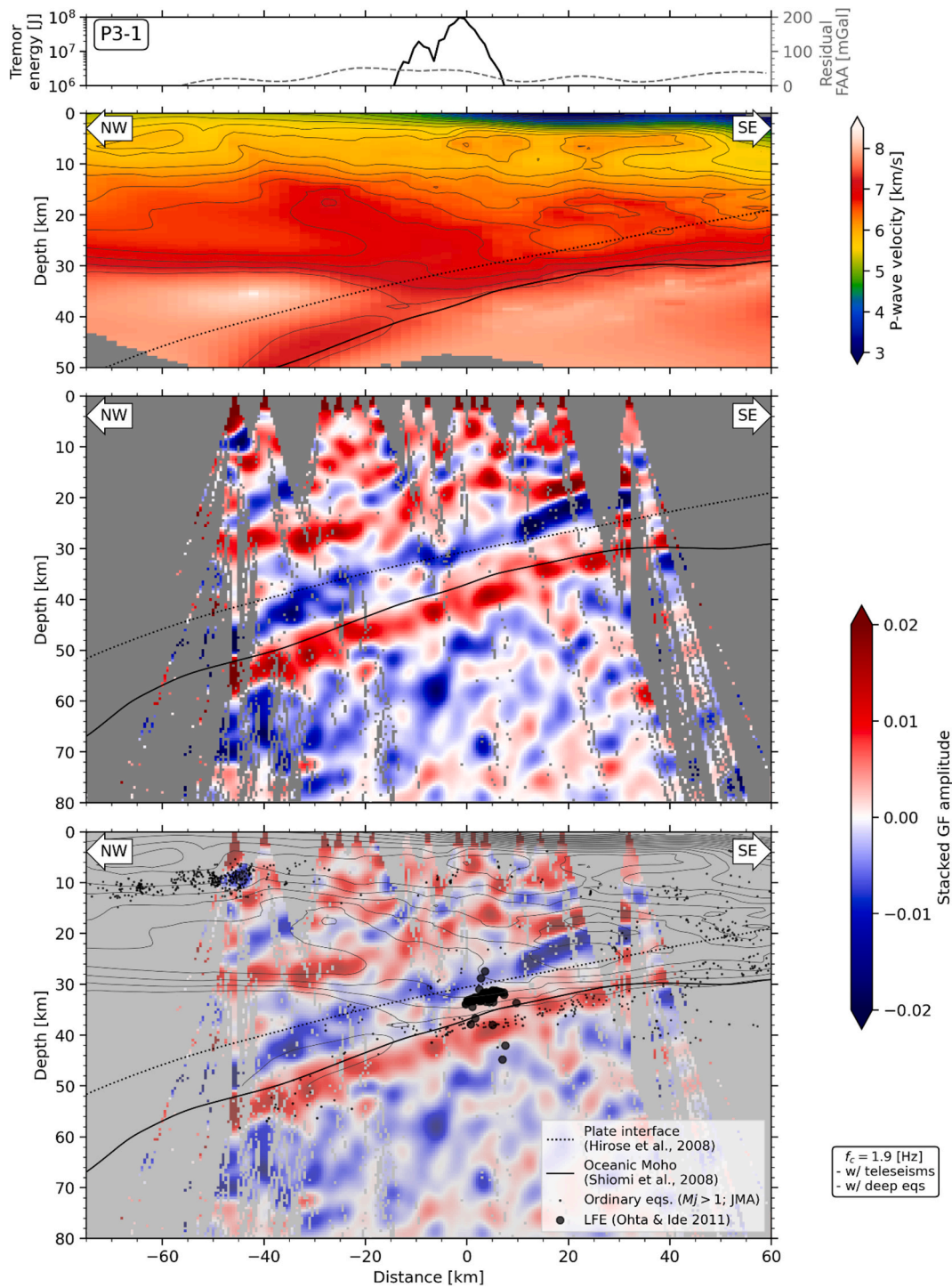


Fig. 8. GF image and P-wave velocity model (Arnulf et al., 2022) in the along-dip profile P3-1. All other details are the same as in Fig. 5.

P4-1 (Fig. S2), we observe positive phases in the forearc crust at a depth of 20–30 km. We could not find any clear phase for the slab top and slab Moho.

5. Discussion

5.1. Fluid supply from the subducting slab

The common feature is the presence of a clear and sharp negative phase for the plate interface. This means that the top of the subducting PHS slab is characterized as a significant low-velocity zone. The

existence of the low-velocity zone at the top of the slab has been demonstrated at various subduction zones (Audet et al., 2009; Kato et al., 2010a; Kim et al., 2014; Pérez-Campos et al., 2008; Sawaki et al., 2021). The amplitude of the negative phases decreases as the slab deepens, which has been modeled as the upper-plate permeability increasing along the transition from the forearc crust to the mantle wedge (Audet et al., 2009; Hansen et al., 2012; Sawaki et al., 2021). Similar to what was shown previously that the updip episodic tremor and LFEs occur around the sharp negative phase at the northeastern Kii Peninsula (Sawaki et al., 2021), sharp negative phases are observed in each along-dip survey line in our study area. This suggests that

impermeable material such as the gabbroic lower forearc crust or high-rigidity rocks overrides the subducting slab where episodic tremor and LFEs take place. The occurrence of short-term SSEs breaks the permeability seal of the overriding forearc crust and allows fluid at near-lithostatic pore pressure to be released toward the upper plate, triggering episodic tremor (e.g., Kita et al., 2021; Nakajima and Uchida, 2018). Taking the cyclic evolution of upper-plate permeability (Nakajima and Uchida, 2018) into consideration, our GF images may show a long-term averaged snapshot of a low-permeability overriding material during inter-SSE periods.

We observed a decrease in the GF amplitude for the slab surface and slab Moho at the downdip portion in the western area (Figs. 5–7), whereas in the eastern area, those phases remain clear even at depth (Fig. 8). The slab dip angle is also steeper in the western section compared with that in the eastern section, which will be discussed in Section 5.3. We attribute this decrease in amplitude to intense eclogitization of the subducting oceanic crust. Eclogitization of oceanic crust releases a lot of fluid (Hacker et al., 2003). Abers et al. (2013) estimated the evolution of lithostatic pressure and slab-released fluid for the western Kii Peninsula, demonstrating a gradual release of fluid from the slab at depths from less than 20 km to 60 km. Significant fluid release occurs at depths of 40–60 km by eclogitization via zoisite and amphibole (Abers et al., 2013). Eclogitization also causes the seismic velocity to gradually increase in the oceanic crust (e.g., Abers, 2005) and makes RF amplitudes decrease (e.g., Abers et al., 2009; Sawaki et al., 2021; Shiomi et al., 2020). An RF image from Kato et al. (2014) also suggested that eclogitization of the oceanic crust results in the disappearance of the slab structure. They explained that eclogitization inverts the polarity of the plate interface phase from negative to positive by increasing the velocity of the oceanic crust. In our study, we observed the decreasing GF amplitude for the slab surface but were unable to trace the slab Moho even at the downdip portion in the western area. The difference in the seismograph distribution and the computation method of RF and GF may differentiate the images of Kato et al. (2014) and ours. However, in both cases, the clear change in the slab structure demonstrates that eclogitization takes place.

Also, the increasing occurrence of intraslab earthquakes is related to the dehydration of the slab (Kita et al., 2006). At the Cascadia subduction zone, the dehydration of the uppermost oceanic mantle triggers intraslab earthquakes, although high pore-fluid pressures alone do not regulate faulting in a slab (Abers et al., 2009). Thus, our GF images imply that eclogitization of oceanic crust taking place beneath the Kii Peninsula leads to the decreasing GF amplitude of the slab around the western to the central area. The increasing number of intraslab earthquakes at the western side may be a proxy of stronger eclogitization of oceanic crust or could be related to serpentinization of oceanic mantle.

Dehydrated fluid would either serpentinize the mantle wedge corner (Kato et al., 2014) or stagnate at the plate interface under high pore-fluid pressure beneath impermeable plutonic bodies, causing LFE and tectonic tremor. Compared to the eastern section, the intense dehydration of the slab could supply an excess of fluid into the tremor zone, potentially resulting in the occurrence of smaller-scale SSEs or aseismic creep. Serpentine, which is altered from mantle peridotite, has a higher permeability by two orders compared with lower crust gabbro (Katayama et al., 2012). So, fluid will eventually infiltrate into the upper plate if the mantle wedge overlies the slab. Alternatively, if impermeable plutonic bodies overlay the slab, fluid will migrate upward along the plate interface. We discuss the overriding lithology in Section 5.2.

Note that our GF images did not exhibit any upwelling structure within the slab mantle. Nakajima and Hasegawa (2007) proposed, based on seismic traveltime tomography, that upwelling mantle fluid from the Pacific slab infiltrates and hydrates the PHS slab in the western Kii region. The presence of deep mantle fluid was supported by the observation of high $^3\text{He}/^4\text{He}$ fluid originating from the deep mantle (Umeda et al., 2006) and might be associated with the generation of LFEs and micro-seismicity. Unfortunately, RF and GF might lack sufficient

sensitivity to a huge structure without a significant velocity contrast if such types of fluid behavior were realistic. Further investigation, involving combined analyses of geology, geochemistry, and seismology, is needed to determine whether the deep mantle fluid is truly upwelling and, if so, what factors significantly contribute to the fluid infiltration into the shallow crust.

5.2. Plutonic bodies and fluid process on subducting PHS slab

In all the along-dip images, the positive phases were also observed in the forearc crust. In the eastern area, the positive phase is almost flat and probably represents the forearc Moho (Sawaki et al., 2021). In contrast, for the central to western areas, the positive velocity contrast rises in the seaward direction (Figs. 5–7). Previous studies with seismic tomography demonstrated notable shallowing of the forearc Moho beneath the southern Kii Peninsula (Katsumata, 2010; Matsubara et al., 2017). However, the positive phases slanted upward do not necessarily indicate the forearc Moho but rather the top interface of some high-velocity body.

Recent tomographic studies demonstrated the presence of a high-velocity body called the Kumano pluton (Arnulf et al., 2022; Nakajima, 2023), based on the high residual free-air gravity anomaly around the southern Kii Peninsula (Bassett and Watts, 2015). The area of high residual free-air gravity anomaly exists beneath the western to central survey lines of P2–1, P1–1, and P2–2 along with the upward-slanting features of positive phases (Figs. 2, 5–8). Considering the residual free-air anomaly in which long-wavelength components have been removed, a high residual free-air gravity anomaly indicates the presence of high-density rock underground. The area of high residual free-air anomaly ($> 60\text{--}70$ mGal) is located around the southern and middle Kii Peninsula in Fig. 2c (Bassett and Watts, 2015). Especially in the southern area, the residual free-air gravity anomaly of the large block exceeds 150 mGal. The high values of Bouguer gravity anomaly extend toward the northern area (Kimura et al., 2014). Those gravity anomalies can be interpreted to indicate that plutonic rocks lie in the noisy positive phases in the forearc crust at the updip of the tectonic tremor band.

Therefore, the observed upward-slanting positive phases lead to two possible interpretations: (a) plutonic bodies are deeply intruded beneath the positive phase; (b) alternatively, the Kumano pluton is confined to a zone near the trench and above the updip portion of the megathrust (Fig. 9). The positive phase in the forearc crust would be the forearc Moho for case (b) but would not be the Moho if the Kumano pluton is deeply intruded for case (a). Specifically, case (b) necessarily implies the existence of the mantle wedge between the forearc Moho and the plate interface. In case (b), the forearc Moho is tilted upward, which could be attributed to regional tectonic forces deforming the accretionary complexes (forearc crust) landward. Kato et al. (2014) suggested the mantle wedge corner would be serpentinized due to fluid leakage by eclogitization of the oceanic crust. Saiga et al. (2013) also suggested that the delay time of trench-parallel S-wave splitting might reflect a 1–15 km thick serpentinite layer with a fully serpentinized mantle wedge. In contrast, Nakajima (2023) disputed the existence of the serpentinized mantle wedge corner because their tomographic results showed a high-velocity anomaly that does not indicate serpentinization. Thus, we interpreted the GF image for the spatial extent of plutonic bodies in two ways (Fig. 9), taking into account that cases (a) and (b) follow interpretations by Nakajima (2023) and Kato et al. (2014), respectively.

We now discuss the possibility of the presence of the serpentinized mantle wedge. We already discussed the dehydration of the subducting slab in Section 5.1. If the mantle wedge corner is serpentinized, the velocity contrast between the slab top and the mantle wedge decreases, and the negative phase of the slab top would be noisy and unclear (e.g., Audet et al., 2009; Sawaki et al., 2021; Shiomi et al., 2020). If the impermeable plutonic body lies on the slab, the negative velocity contrast from the high pore-fluid pressure oceanic crust to the overriding high-velocity Kumano pluton remains large in a narrow area

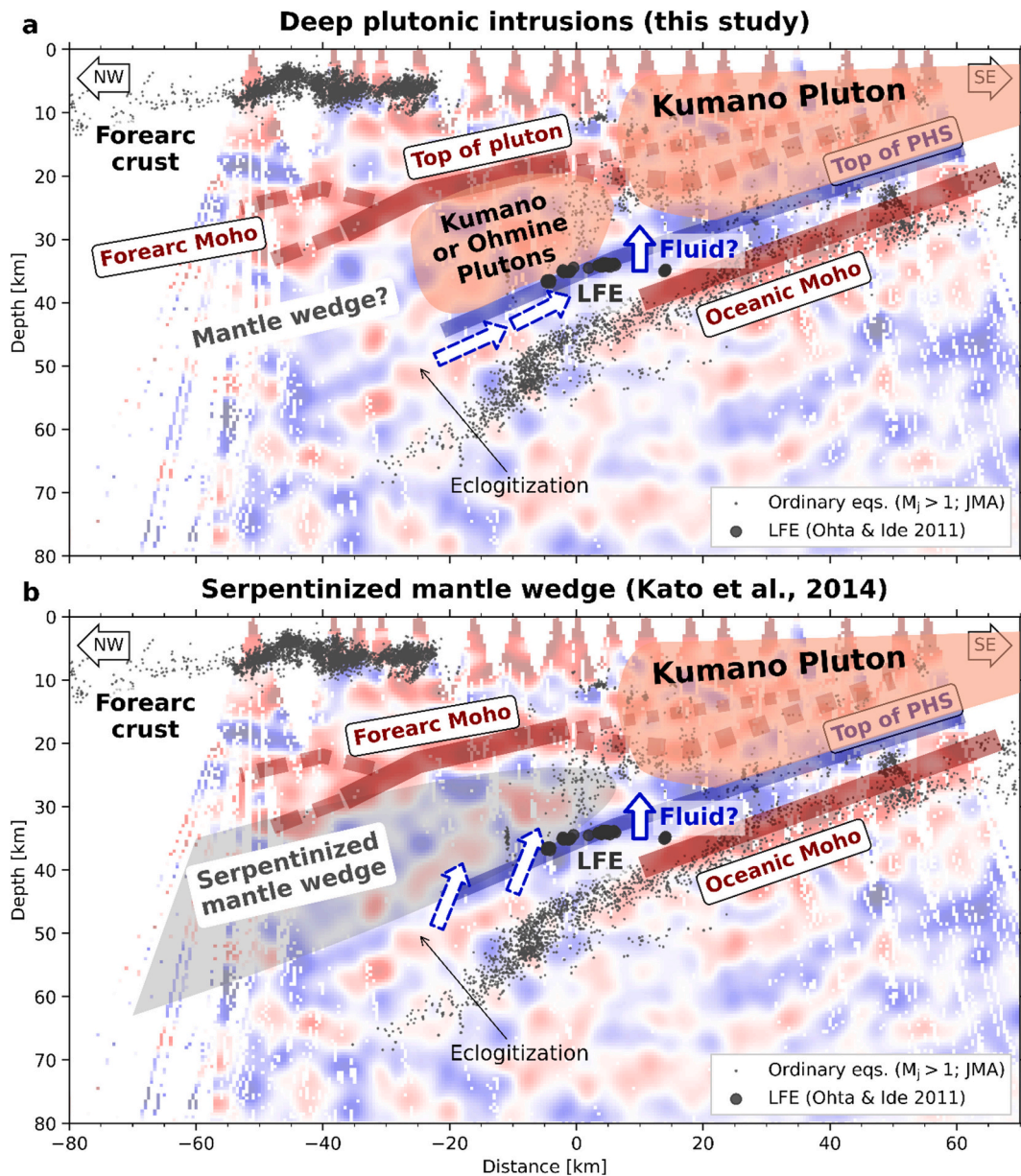


Fig. 9. Schematic illustrations over the GF image in the along-dip profile P2-1. (a) Model for deeply-intruded plutonic bodies, based on Kimura et al. (2014) and Nakajima (2023). (b) Model for serpentinized mantle wedge based on Kato et al. (2014) and Kumano pluton confined updip.

around the plate interface. The negative phase in GF images is rather sharp at the downdip side of LFE sources. Also, we did not confirm the presence of an inverted Moho or unclear Moho, which have been observed at Cascadia (Bostock et al., 2002), Tokai (Kato et al., 2010a), and western Shikoku (Shiomi et al., 2020). As an inverted Moho often represents a highly serpentinized mantle wedge (Bostock et al., 2002), the positive phase tilted upward in the forearc side does not necessarily indicate the existence of the serpentinized mantle wedge corner. Taking into account the observations of gravity anomaly, intraslab seismicity, and RF/GF phases, our interpretation leans towards the idea that plutonic bodies extend deep beneath the forearc crust as well as laterally over the subducting PHS slab at the western Kii Peninsula (Fig. 9a).

Within the context of the deeply intruded plutonic bodies, the positive phase tilted upward accounts for the upper surface of the pluton (Fig. 9a). Despite diminishing clarity due to a decrease in ray hit counts, the positive phase on the forearc side continues to show the slanted-up feature. The phase is likely linked to the forearc Moho, estimated by previous observations (e.g., Katsumata, 2010; Matsubara et al., 2017).

Consequently, we infer that the positive phase tilted upward represents the forearc Moho on the forearc side and the upper surface of the plutonic bodies on the shallower side of the plate subduction.

A segment of a strong negative phase was seen in the GF image around the shallower edge of the arched shape at 20 km depth at the horizontal location of 20 km (Fig. 5). This negative phase is generally considered to represent the slab surface but extends shallower toward the forearc crust, located beneath a relatively higher P-wave velocity area (Arnulf et al., 2022). Additionally, the crustal seismicity at the updip side of LFE sources is noteworthy. An arched distribution of micro-seismicity is evident at the depth between 20 and 30 km around the horizontal location between 0 and 30 km (Fig. 5). A similar feature was observed in tomographic studies. Kato et al. (2014) showed a negative P- and S-wave velocity anomaly around this region, suggesting fluid leakage from the oceanic crust to the forearc crust. Nakajima (2023) interpreted this portion as the bottom at the northern end of the high-velocity Kumano pluton. Also, P-wave attenuation structure suggests that the overriding material in the western side is rather permeable

compared to the eastern side (Kita and Matsubara, 2016). The trench-parallel fast axis and the delay time of S-wave splitting are also dominant compared to the eastern area (Imanishi et al., 2016; Nakajima and Hasegawa, 2016; Saiga et al., 2013). Provided that the low-velocity anomaly reflects a locally permeable condition over the slab, microseismicity might occur due to fluid diffusion under well-drained conditions (Nakajima and Hasegawa, 2016).

Furthermore, around the middle of the Kii Peninsula, intrusions of Ohmine rocks in the middle Miocene have been found (Shinjoe et al., 2005). Considering that the positive Bouguer gravity anomaly extends north of the tectonic tremor band (Kimura et al., 2014), deeper intrusion of Ohmine granitic rocks is also a possible scenario (Fig. 9a). Magnetotelluric analysis inferred that the Kumano pluton and Ohmine pluton adjoin at depth (Umeda et al., 2003). However, the extent to which the Kumano pluton and Ohmine pluton are interconnected remains uncertain. If the Ohmine pluton lies over the deeper slab instead of the Kumano pluton and those two bodies are partially separated (Kimura et al., 2014), the space between those plutonic bodies would result in a small-scale increase in permeability (Fig. 9a). We speculate that the fluid along the plate interface could potentially infiltrate the overriding Kumano pluton through zones of fracturing with locally high permeability. Another possible explanation is that fluid might be trapped within an unreported subducted seamount, though we do not have clear evidence.

To summarize the discussion, case (a) with deeply intruded plutonic bodies is the most suitable explanation for seismotectonics in the western and central Kii Peninsula (Fig. 9a). Broader aspects of geophysical and geological studies are necessary for further discussion.

5.3. Complex slab geometry around the western area

The stress state and slab geometry in the western area are complex. Otsubo et al. (2019) estimated the spatial variation of intraslab stress around the Kii and Shikoku regions and suggested that triaxial normal faulting stress may control the tendency of fluid release and migration in the slab. Uchide et al. (2022) showed that the horizontal maximum compressional axis is oriented along the E–W direction, consistent with the S-wave fast axis estimated by Saiga et al. (2013). In contrast, the compressional azimuth in the central area faces the NE–SW direction (Uchide et al., 2022), so the stress state undergoes significant spatial changes. Also, the PHS slab shows a valley-like shape around the western area (Hirose et al., 2008; Shiomi et al., 2008), and the subduction azimuth of NW–SE may not be perpendicular to the strike of the subducted slab (Shiomi and Park, 2008). Furthermore, intraslab earthquakes show a steeper alignment as the slab deepens (Fig. 9). These observations suggest that the slab geometry gets steeper and that the survey line P2–1 might not partially be the along-dip cross-section. Also, imaging a high-angle structure is not straightforward using RF or GF. Because the existence of the overriding plutonic bodies at least affects the slab curvature (Arnulf et al., 2022), it is possible that the change in slab bending or the complicated slab geometry would make GF phases vague or complex.

The along-strike variation in the background seismicity or the slip characteristics may reflect the complexity of the slab geometry regarding the plutonic bodies. The background seismicity rate is high at the westernmost Kii Peninsula, where less tectonic tremor energy is released (Mitsui et al., 2022). Large long-term SSEs have been detected in this region (e.g., Kobayashi, 2017), although no significant events occur in the Kii Peninsula except in the shallower portion of the northeastern area (Kobayashi and Tsuyuki, 2019). The cumulative slip of short-term SSEs also exhibits notable spatial variation, and a smaller number of events have occurred in the western area (Fig. 2f) (Okada et al., 2022). A steeper dip angle of the slab and its complex geometry could increase the supply into the plate interface of the dehydrated fluid per unit of the along-dip distance. Such an excess of fluid into the tremor zone might result in the occurrence of smaller-scale SSEs or aseismic

creep. The plutonic bodies, also revealed by the spatial variation of GF phases, could dominate slip behavior around the plate interface.

5.4. Other seismic structures potentially linked to slow and fast earthquakes

The source environment of LFEs at the northeastern Kii Peninsula is under debate. Kurashimo et al. (2021) performed a seismic reflection analysis of crustal earthquakes around our P3–1 line. Their result clearly showed the reflection from the plate interface, and the depth of the main reflection was consistent with our GF negative phase for the plate interface, while we did not observe any significant southward-dipping velocity contrast that they observed as the strong reflector (Fig. S3). Relocated LFEs by Kurashimo et al. (2021) are mainly located around the positive phase for the slab Moho and are on the slab Moho model by Shiomi et al. (2008). Kurashimo et al. (2021) claimed that intraslab LFEs are located beneath the oceanic Moho and are controlled by fluid migration due to the serpentinization of the slab mantle. Their assumption that the oceanic Moho is located 7.5 km beneath the plate interface does not properly reflect the spatial geometry of the subducting slab, and our result does not support the presence of intraslab LFEs beneath the slab Moho. In contrast, LFEs relocated by the network correlation coefficient method are mostly several kilometers beneath the plate interface but are significantly above the slab Moho (Ohta and Ide, 2011). The inconsistency probably comes from the difference in the relocation method and the velocity model. Another possible theory is that intraslab LFEs occur beneath a thickened and detached reflective slab (Bloch et al., 2023). Regardless, determining the exact location of LFEs is not a straightforward task, given that LFEs were not relocated using the velocity model by Matsubara et al. (2022). However, it is an important future task to constrain the source environment of slow earthquakes through various geophysical analyses.

In the P3–1 line, successive positive and negative phases were observed tilting upward in the forearc crust, which could be related to the deep extension of the Median Tectonic Line dipping toward the north (Kurashimo et al., 2021) (Fig. S3). The Sanbagawa metamorphic belt is located at the northern edge of the Outer Zone in Southwestern Japan and is formed from high-pressure crystalline schist. While passive seismic sources have poor resolution for highly dipping structures, a related feature of successive RF phases was also observed beneath the Tokai area (Kato et al., 2010a). Although no clear velocity gradient was observed from the P-wave tomography (Arnulf et al., 2022), the transition of geological structure might contribute to such a shallow velocity contrast.

In the northwestern area, prominent non-volcanic earthquake swarms, known collectively as the Wakayama swarm, have been observed (e.g., Kato et al., 2010b; Mizoue et al., 1983). We did not observe a clear feature in the GF image along the P2–1 line around 10 km depth (Fig. 5), as passive sources may not provide high-frequency signals sufficient to resolve such a shallow structure. Kato et al. (2010b) imaged a high-velocity body just beneath the swarm activities around 6–9 km depth and inferred that fluid processes induced by the thermal effect of solidified intruded magma may trigger the swarms. Other tomographic studies found a low-velocity anomaly below the swarm at 10–20 km (Kato et al., 2014; Nakajima, 2023). Also, later phases in earthquake coda waves may contain information to constrain the crustal structure (Shiina et al., 2024). Velocity discontinuities have been estimated by extracting reflected waves (Mizoue, 1971) and Sp phases (Doi and Kawakata, 2013). Doi and Kawakata (2013) observed subsurface velocity contrasts such as the Conrad discontinuity and forearc Moho. They also found another Sp conversion at depths of 8–13 km above the Conrad, just beneath the Wakayama swarm. Combining seismic tomography, later phases in earthquake coda waves, and broader-band GF analysis will help to better constrain spatial features such as igneous intrusions from shallow to deep areas and elucidate the geophysical model of related subduction zone seismicity.

6. Conclusions

Images of receiver-side Green's functions up to 2 Hz at the Kii Peninsula revealed a sharp negative S-wave velocity contrast on the top surface of the subducting Philippine Sea plate and a positive phase tilted upward in the forearc crust. In the eastern area, we observe a sharp negative phase on the top surface of the subducting slab. This suggests that the forearc crust is on the top of the slab and above the zone of low frequency earthquakes and tectonic tremors. The noisy negative phase in the downdip portion indicates the presence of the serpentinized mantle wedge corner. The low-permeability of the forearc crust prevents the slab-dehydrated fluid from infiltrating into the upper plate. In the western area, we noted sharp negative phases for the slab surface and positive phases slanted upward in the forearc crust. Studies of gravity anomaly and seismic tomography have demonstrated the broad presence of high-density and high-velocity igneous bodies of the Kumano pluton broadly in the forearc crust. The upward-slanting positive phase likely represents the top surface of plutonic bodies that span all the way down to the plate interface. The sharp negative phase extends towards the deeper extent of slow-earthquake sources. Together with the observations of gravity anomaly, intraslab seismicity, and seismic tomography, the interpretation of our results supports the presence of plutonic bodies which extend deep beneath the forearc crust as well as laterally over the subducting PHS slab, rather than a serpentinized mantle wedge at the western Kii Peninsula. The upper plate is generally low in permeability. However, as confirmed by the partial presence of low seismic wave velocities, a segment of negative phases and the arch-like pattern of crustal seismicity may suggest areas of high permeability on the updip side of the sources of low-frequency earthquakes and tectonic tremors. The condition in which fluid can locally infiltrate upwards is speculated to maintain the relatively less active slow earthquakes in the western area. The lateral variation of the upper-plate lithology likely influences fluid processes and slow earthquake activities.

CRedit authorship contribution statement

Yasunori Sawaki: Writing – review & editing, Writing – original draft, Visualization, Validation, Software, Investigation, Funding acquisition, Formal analysis, Data curation, Conceptualization. **Yoshihiro Ito:** Writing – review & editing, Supervision, Resources, Funding acquisition. **Emmanuel Soliman M. Garcia:** Writing – review & editing, Visualization. **Ayumu Miyakawa:** Writing – review & editing. **Takuo Shibutani:** Writing – review & editing, Resources, Funding acquisition, Data curation.

Declaration of competing interest

The authors declare that they have no known competing financial interests or personal relationships that could have appeared to influence the work reported in this paper.

Data availability

The Fortran program for computing receiver-side Green's functions by [Akuhara et al. \(2019\)](#) is available at GitHub repository (<https://github.com/akuhara/MC3deconv>) or at Zenodo repository ([Akuhara, 2019](#)). The 3-D seismic velocity model ALJ.2023 ([Matsubara et al., 2022](#)) is available at the Japanese website of the National Research Institute for Earth Science and Disaster Resilience (NIED) Hinet (https://www.hinet.bosai.go.jp/topics/sokudo_kozo/alljpn_download.php), last accessed in October 2023. We fetched the geological data from the Seamless Digital Geological Map of Japan V2 1:200,000 ([Geological Survey of Japan AIST, 2022](#)) (<https://gbank.gsj.jp/seamless/> last accessed on October 3, 2023). The waveform data will be made available on reasonable request.

Acknowledgments

We acknowledge the editor Liang Zhao and two anonymous reviewers for their constructive feedback. We would like to thank the staff involved in the campaign-type linear array seismic observations in the Kii Peninsula from March 2004 to March 2013, operated by DPRI, Kyoto University, Japan. We are deeply grateful to Katsuhiko Shiomi for providing us the PHS slab Moho model ([Shiomi et al., 2008](#)). A special gratitude we give to Kazuaki Ohta for providing us the source location of low-frequency earthquakes ([Ohta and Ide, 2011](#)). We also offer our thanks to Yutaro Okada for fruitful discussion and sharing processed data of short-term SSEs ([Okada et al., 2022](#)). We also had illuminating discussions with Kodai Sagae, Takahiro Shiina, Yuta Amezawa, David Shelly, Sando Sawa, Yihuan Ruan, Shukei Ohyanagi, Takeshi Akuhara, and Kazushige Obara. We processed seismic recordings using ObsPy (e.g. [Beyreuther et al., 2010](#)). Source information for regional deep-focus earthquake events from the Japan Meteorological Agency (JMA) Unified Earthquake Catalog (https://www.data.jma.go.jp/svd/eqev/dat/bulletin/index_e.html), which was last accessed in March 2024. Similarly, we retrieved source information for teleseismic events from the United States Geological Survey (USGS) Earthquake Catalog (<https://earthquake.usgs.gov/>), also last accessed in March 2024. For visualization purposes, we utilized Matplotlib ([Hunter, 2007](#)) and GMT6 ([Wessel et al., 2019](#)) through its Python wrapper, PyGMT 0.10.0 ([Tian et al., 2023](#)). This study was supported by the Ministry of Education, Culture, Sports, Science and Technology (MEXT) of Japan, under the Special Project for Earthquake Disaster Mitigation in Urban Areas and the Earthquake and Volcano Hazards Observation and Research Program (Earthquake and Volcano Hazard Reduction Research). This work was funded by MEXT KAKENHI Grant-in-Aid for Transformative Research Areas (A) “Science of Slow-to-Fast Earthquakes” (Grant Numbers JP21H05203 and JP22H05316). YS was also supported by JST SPRING (Grant Number JPMJSP2110) and by JSPS KAKENHI Grant-in-Aid for Research Activity Start-up (Grant Number JP23K19077).

Appendix A. Supplementary data

Supplementary data to this article can be found online at <https://doi.org/10.1016/j.tecto.2024.230536>.

References

- Abers, G.A., 2005. Seismic low-velocity layer at the top of subducting slabs: observations, predictions, and systematics. *Phys. Earth Planet. Inter.* 149, 7–29. <https://doi.org/10.1016/j.pepi.2004.10.002>.
- Abers, G.A., Mackenzie, L.S., Rondenay, S., Zhang, Z., Wech, A.G., Creager, K.C., 2009. Imaging the source region of Cascadia tremor and intermediate-depth earthquakes. *Geology* 37, 1119–1122. <https://doi.org/10.1130/G30143A.1>.
- Abers, G.A., Nakajima, J., van Keken, P.E., Kita, S., Hacker, B.R., 2013. Thermal-petrological controls on the location of earthquakes within subducting plates. *Earth Planet. Sci. Lett.* 369–370, 178–187. <https://doi.org/10.1016/j.epsl.2013.03.022>.
- Akuhara, T., 2019. Multichannel deconvolution by reversible-jump Markov-chain Monte Carlo (MC3deconv v1.0.1). <https://doi.org/10.5281/zenodo.2548974>.
- Akuhara, T., Mochizuki, K., Kawakatsu, H., Takeuchi, N., 2017. A fluid-rich layer along the Nankai trough megathrust fault off the Kii Peninsula inferred from receiver function inversion. *J. Geophys. Res. Solid Earth* 122, 6524–6537. <https://doi.org/10.1002/2017JB013965>.
- Akuhara, T., Bostock, M.G., Plourde, A.P., Shinohara, M., 2019. Beyond receiver functions: Green's function estimation by transdimensional inversion and its application to OBS data. *J. Geophys. Res. Solid Earth* 124, 1944–1961. <https://doi.org/10.1029/2018JB016499>.
- Akuhara, T., Tsuji, T., Tonegawa, T., 2020. Overpressured underthrust sediment in the Nankai trough forearc inferred from transdimensional inversion of high-frequency teleseismic waveforms. *Geophys. Res. Lett.* 47, e2020GL088280. <https://doi.org/10.1029/2020GL088280>.
- Akuhara, T., Yamashita, Y., Ohyanagi, S., Sawaki, Y., Yamada, T., Shinohara, M., 2023. Shallow low-velocity layer in the Hyuga-Nada accretionary prism and its hydrological implications: insights from passive seismic array. *J. Geophys. Res. Solid Earth* 128, e2022JB026298. <https://doi.org/10.1029/2022JB026298>.
- Ammon, C.J., 1991. The isolation of receiver effects from teleseismic P waveforms. *Bull. Seismol. Soc. Am.* 81, 2504–2510. <https://doi.org/10.1029/2005JB004161>.

- Annoura, S., Obara, K., Maeda, T., 2016. Total energy of deep low-frequency tremor in the Nankai subduction zone, southwest Japan. *Geophys. Res. Lett.* 43, 2562–2567. <https://doi.org/10.1002/2016GL067780>.
- Arnulf, A.F., Bassett, D., Harding, A.J., Kodaira, S., Nakanishi, A., Moore, G., 2022. Upper-plate controls on subduction zone geometry, hydration and earthquake behaviour. *Nat. Geosci.* 15, 143–148. <https://doi.org/10.1038/s41561-021-00879-x>.
- Audet, P., Kim, Y., 2016. Teleseismic constraints on the geological environment of deep episodic slow earthquakes in subduction zone forearcs: A review. *Tectonophysics* 670, 1–15. <https://doi.org/10.1016/j.tecto.2016.01.005>.
- Audet, P., Bostock, M.G., Christensen, N.I., Peacock, S.M., 2009. Seismic evidence for overpressured subducted oceanic crust and megathrust fault sealing. *Nature* 457, 76–78. <https://doi.org/10.1038/nature07650>.
- Bassett, D., Watts, A.B., 2015. Gravity anomalies, crustal structure, and seismicity at subduction zones: 2. Interrelationships between fore-arc structure and seismogenic behavior. *Geochemistry. Geophys. Geosyst.* 16, 1541–1576. <https://doi.org/10.1002/2014GC005685>.
- Bassett, D., Arnulf, A., Kodaira, S., Nakanishi, A., Harding, A., Moore, G., 2022. Crustal structure of the Nankai subduction zone revealed by two decades of onshore-offshore and ocean-bottom seismic data: implications for the dimensions and slip behavior of the seismogenic zone. *J. Geophys. Res. Solid Earth* 127, e2022JB024992. <https://doi.org/10.1029/2022JB024992>.
- Beyreuther, M., Barsch, R., Krischer, L., Megies, T., Behr, Y., Wassermann, J., 2010. ObsPy: A python toolbox for seismology. *Seismol. Res. Lett.* 81, 530–533. <https://doi.org/10.1785/gssrl.81.3.530>.
- Bloch, W., Bostock, M.G., Audet, P., 2023. A Cascadia slab model from receiver functions. *Geochem. Geophys. Geosyst.* 24, e2023GC011088. <https://doi.org/10.1029/2023GC011088>.
- Bostock, M.G., Hyndman, R.D., Rondenay, S., Peacock, S.M., 2002. An inverted continental moho and serpentinization of the forearc mantle. *Nature* 417, 536–538. <https://doi.org/10.1038/417536a>.
- Crotwell, H.P., Owens, T.J., Ritsema, J., 1999. The TauP toolkit: flexible seismic travel-time and ray-path utilities. *Seismol. Res. Lett.* 70, 154–160. <https://doi.org/10.1785/gssrl.70.2.154>.
- Doi, I., Kawakata, H., 2013. High resolution spatial distribution of the velocity discontinuities in and around the swarm region beneath the Wakayama district, southwest Japan. *Bull. Seismol. Soc. Am.* 103, 2135–2141. <https://doi.org/10.1785/0120120316>.
- Dueker, K.G., Sheehan, A.F., 1997. Mantle discontinuity structure from midpoint stacks of converted P to S waves across the Yellowstone hotspot track. *J. Geophys. Res. Solid Earth* 102, 8313–8327. <https://doi.org/10.1029/96jb03857>.
- Egbert, G.D., Yang, B., Bedrosian, P.A., Key, K., Livelybrooks, D.W., Schultz, A., Kelbert, A., Parris, B., 2022. Fluid transport and storage in the Cascadia forearc influenced by overriding plate lithology. *Nat. Geosci.* 15, 677–682. <https://doi.org/10.1038/s41561-022-00981-8>.
- Geological Survey of Japan AIST, 2022. Seamless digital geological map of Japan V2 1: 200,000 [WWW Document]. URL <https://gbank.gsj.jp/seamless/> (accessed 10.3.23).
- Green, P.J., 1995. Reversible jump Markov chain Monte Carlo computation and Bayesian model determination. *Biometrika* 82, 711–732. <https://doi.org/10.1093/biomet/82.4.711>.
- Hacker, B.R., Peacock, S.M., Abers, G.A., Holloway, S.D., 2003. Subduction factory 2. Are intermediate-depth earthquakes in subducting slabs linked to metamorphic dehydration reactions? *J. Geophys. Res. Solid Earth* 108. <https://doi.org/10.1029/2001JB001129>.
- Hansen, R.T.J., Bostock, M.G., Christensen, N.I., 2012. Nature of the low velocity zone in Cascadia from receiver function waveform inversion. *Earth Planet. Sci. Lett.* 337–338, 25–38. <https://doi.org/10.1016/j.epsl.2012.05.031>.
- Hirose, F., Nakajima, J., Hasegawa, A., 2008. Three-dimensional seismic velocity structure and configuration of the Philippine Sea slab in southwestern Japan estimated by double-difference tomography. *J. Geophys. Res. Solid Earth* 113, B09315. <https://doi.org/10.1029/2007JB005274>.
- Honda, R., Kono, Y., 2005. Buried large block revealed by gravity anomalies in the Tonankai and Nankai earthquake regions, southwestern Japan. *Earth Planets Space* 57, e1–e4. <https://doi.org/10.1186/BF03351799>.
- Hunter, J.D., 2007. Matplotlib: A 2D Graphics Environment. *Comput. Sci. Eng.* 9, 90–95. <https://doi.org/10.1109/MCSE.2007.55>.
- Ide, S., Beroza, G.C., 2023. Slow earthquake scaling reconsidered as a boundary between distinct modes of rupture propagation. *Proc. Natl. Acad. Sci.* 120. <https://doi.org/10.1073/pnas.2222102120>.
- Imanishi, K., Uchide, T., Takeda, N., 2016. Determination of focal mechanisms of nonvolcanic tremor using S wave polarization data corrected for the effects of anisotropy. *Geophys. Res. Lett.* 43, 611–619. <https://doi.org/10.1002/2015GL067249>.
- Ito, Y., Hino, R., Kido, M., Fujimoto, H., Osada, Y., Inazu, D., Ohta, Y., Iinuma, T., Ohzono, M., Miura, S., Mishina, M., Suzuki, K., Tsuji, T., Ashi, J., 2013. Episodic slow slip events in the Japan subduction zone before the 2011 Tohoku-Oki earthquake. *Tectonophysics* 600, 14–26. <https://doi.org/10.1016/j.tecto.2012.08.022>.
- Kanasewich, E.R., Hemmings, C.D., Alpaslan, T., 1973. Nth-root stack nonlinear multichannel filter. *Geophysics* 38, 327–338. <https://doi.org/10.1190/1.1440343>.
- Katayama, I., Terada, T., Okazaki, K., Tanikawa, W., 2012. Episodic tremor and slow slip potentially linked to permeability contrasts at the Moho. *Nat. Geosci.* 5, 731–734. <https://doi.org/10.1038/ngeo1559>.
- Kato, A., Iidaka, T., Ikuta, R., Yoshida, Y., Katsumata, K., Iwasaki, T., Sakai, S., Thurber, C., Tsumura, N., Yamaoka, K., Watanabe, T., Kunitomo, T., Yamazaki, F., Okubo, M., Suzuki, S., Hirata, N., 2010a. Variations of fluid pressure within the subducting oceanic crust and slow earthquakes. *Geophys. Res. Lett.* 37, L14310. <https://doi.org/10.1029/2010GL043723>.
- Kato, A., Sakai, S., Iidaka, T., Iwasaki, T., Hirata, N., 2010b. Non-volcanic seismic swarms triggered by circulating fluids and pressure fluctuations above a solidified diorite intrusion. *Geophys. Res. Lett.* 37, L15302. <https://doi.org/10.1029/2010GL043887>.
- Kato, A., Obara, K., Igarashi, T., Tsuruoka, H., Nakagawa, S., Hirata, N., 2012. Propagation of slow slip leading up to the 2011 Mw9.0 Tohoku-Oki earthquake. *Science* 335, 705–708. <https://doi.org/10.1126/science.1215141>.
- Kato, A., Saiga, A., Takeda, T., Iwasaki, T., Matsuzawa, T., 2014. Non-volcanic seismic swarm and fluid transportation driven by subduction of the Philippine Sea slab beneath the Kii Peninsula, Japan. *Earth Planets Space* 66, 86. <https://doi.org/10.1186/1880-5981-66-86>.
- Katsumata, A., 2010. Depth of the Moho discontinuity beneath the Japanese islands estimated by traveltime analysis. *J. Geophys. Res. Solid Earth* 115, B04303. <https://doi.org/10.1029/2008JB005864>.
- Kim, Y., Abers, G.A., Li, J., Christensen, D., Calkins, J., Rondenay, S., 2014. Alaska Megathrust 2: Imaging the megathrust zone and Yakutat/Pacific plate interface in the Alaska subduction zone. *J. Geophys. Res. Solid Earth* 119, 1924–1941. <https://doi.org/10.1002/2013JB010581>.
- Kimura, G., Hashimoto, Y., Kitamura, Y., Yamaguchi, A., Koge, H., 2014. Middle Miocene swift migration of the TTT triple junction and rapid crustal growth in southwest Japan: A review. *Tectonics* 33, 1219–1238. <https://doi.org/10.1002/2014TC003531>.
- Kimura, G., Nakamura, Y., Shiraishi, K., Fujie, G., Kodaira, S., Tsuji, T., Fukuchi, R., Yamaguchi, A., 2022. Nankai forearc structural and seismogenic segmentation caused by a magmatic intrusion off the Kii Peninsula. *Geochem. Geophys. Geosyst.* 23, e2022GC010331. <https://doi.org/10.1029/2022GC010331>.
- Kita, S., Matsubara, M., 2016. Seismic attenuation structure associated with episodic tremor and slip zone beneath Shikoku and the Kii peninsula, southwestern Japan, in the Nankai subduction zone. *J. Geophys. Res. Solid Earth* 121, 1962–1982. <https://doi.org/10.1002/2015JB012493>.
- Kita, S., Okada, T., Nakajima, J., Matsuzawa, T., Hasegawa, A., 2006. Existence of a seismic belt in the upper plane of the double seismic zone extending in the along-arc direction at depths of 70–100 km beneath NE Japan. *Geophys. Res. Lett.* 33, L24310. <https://doi.org/10.1029/2006GL028239>.
- Kita, S., Houston, H., Yabe, S., Tanaka, S., Asano, Y., Shibutani, T., Suda, N., 2021. Effects of episodic slow slip on seismicity and stress near a subduction-zone megathrust. *Nat. Commun.* 12, 7253. <https://doi.org/10.1038/s41467-021-27453-8>.
- Kobayashi, A., 2017. Objective detection of long-term slow slip events along the Nankai Trough using GNSS data (1996–2016). *Earth Planets Space* 69. <https://doi.org/10.1186/s40623-017-0755-7>.
- Kobayashi, A., Tsuyuki, T., 2019. Long-term slow slip event detected beneath the Shima Peninsula, central Japan, from GNSS data. *Earth Planets Space* 71, 60. <https://doi.org/10.1186/s40623-019-1037-3>.
- Kodaira, S., Hori, T., Ito, A., Miura, S., Fujie, G., Park, J., Baba, T., Sakaguchi, H., Kameda, Y., 2006. A cause of rupture segmentation and synchronization in the Nankai trough revealed by seismic imaging and numerical simulation. *J. Geophys. Res. Solid Earth* 111, B09301. <https://doi.org/10.1029/2005JB004030>.
- Kolb, J.M., Leki, V., 2014. Receiver function deconvolution using transdimensional hierarchical Bayesian inference. *Geophys. J. Int.* 197, 1719–1735. <https://doi.org/10.1093/gji/ggu079>.
- Kurashimo, E., Iwasaki, T., Tsumura, N., Iidaka, T., 2021. The role of fluid-related heterogeneous structures in controlling the fault slip behavior in the slow-earthquake source region along the Nankai subduction zone, southwest Japan. *Geophys. Res. Lett.* 48, e2020GL089882. <https://doi.org/10.1029/2020GL089882>.
- Langston, C.A., 1979. Structure under Mount Rainier, Washington, inferred from teleseismic body waves. *J. Geophys. Res.* 84, 4749–4762. <https://doi.org/10.1029/JB084iB09p04749>.
- Leah, H., Fagereng, Å., Bastow, I., Bell, R., Lane, V., Henrys, S., Jacobs, K., Fry, B., 2022. The northern Hikurangi margin three-dimensional plate interface in New Zealand remains rough 100 km from the trench. *Geology* 50, 1256–1260. <https://doi.org/10.1130/G50272.1>.
- Ligorria, J.P., Ammon, C.J., 1999. Iterative deconvolution and receiver-function estimation. *Bull. Seismol. Soc. Am.* 89, 1395–1400. <https://doi.org/10.1785/BSSA0890051395>.
- Matsubara, M., Sato, H., Ishiyama, T., Van Horne, A., 2017. Configuration of the Moho discontinuity beneath the Japanese Islands derived from three-dimensional seismic tomography. *Tectonophysics* 710–711, 97–107. <https://doi.org/10.1016/j.tecto.2016.11.025>.
- Matsubara, M., Ishiyama, T., No, T., Uehira, K., Mochizuki, M., Kanazawa, T., Takahashi, N., Kamiya, S., 2022. Seismic velocity structure along the Sea of Japan with large events derived from seismic tomography for whole Japanese Islands including reflection survey data and NIED MOWLAS Hi-net and S-net data. *Earth Planets Space* 74, 171. <https://doi.org/10.1186/s40623-022-01724-0>.
- Mitsui, Y., Uehara, K., Kosugi, I., Matsuo, K., 2022. Along-strike distribution of seismicity and large slow slip correlated with gravity at the Nankai Trough. *Earth Planet. Sci. Lett.* 598, 117824. <https://doi.org/10.1016/j.epsl.2022.117824>.
- Mizoue, M., 1971. Crustal structure from travel times of reflected and refracted seismic waves recorded at Wakayama Micro-earthquake Observatory and its substations. *Bull. Earthq. Res. Inst.* 49, 33–62. <https://doi.org/10.15083/0000033259>.
- Mizoue, M., Nakamura, M., Seto, N., Ishiketa, Y., Yokota, T., 1983. Three-layered distribution of microearthquakes in relation to focal mechanism variation in the Kii Peninsula, southwestern Honshu. *Bull. Earthq. Res. Inst.* 58, 287–310. <https://doi.org/10.15083/0000032951>.

- Muirhead, K.J., 1968. Eliminating false alarms when detecting seismic events automatically. *Nature* 217, 533–534. <https://doi.org/10.1038/217533a0>.
- Nakajima, J., 2023. The Wakayama earthquake swarm in Japan. *Earth Planets Space* 75, 48. <https://doi.org/10.1186/s40623-023-01807-6>.
- Nakajima, J., Hasegawa, A., 2006. Anomalous low-velocity zone and linear alignment of seismicity along it in the subducted Pacific slab beneath Kanto, Japan: Reactivation of subducted fracture zone? *Geophys. Res. Lett.* 33, L16309. <https://doi.org/10.1029/2006GL026773>.
- Nakajima, J., Hasegawa, A., 2007. Tomographic evidence for the mantle upwelling beneath southwestern Japan and its implications for arc magmatism. *Earth Planet. Sci. Lett.* 254, 90–105. <https://doi.org/10.1016/j.epsl.2006.11.024>.
- Nakajima, J., Hasegawa, A., 2016. Tremor activity inhibited by well-drained conditions above a megathrust. *Nat. Commun.* 7, 13863. <https://doi.org/10.1038/ncomms13863>.
- Nakajima, J., Uchida, N., 2018. Repeated drainage from megathrusts during episodic slow slip. *Nat. Geosci.* 11, 351–356. <https://doi.org/10.1038/s41561-018-0090-z>.
- Nakajima, J., Hirose, F., Hasegawa, A., 2009. Seismotectonics beneath the Tokyo metropolitan area, Japan: Effect of slab-slab contact and overlap on seismicity. *J. Geophys. Res.* 114, B08309. <https://doi.org/10.1029/2008JB006101>.
- Nishikawa, T., Ide, S., Nishimura, T., 2023. A review on slow earthquakes in the Japan Trench. *Prog. Earth Planet Sci.* 10, 1. <https://doi.org/10.1186/s40645-022-00528-w>.
- Nishimura, K., Nakao, S., Tatsumi, K., Miura, T., Hirano, N., Yamazaki, T., Tomisaka, K., Fukushima, M., Yoshida, Y., Hoso, Y., Matsuura, H., Shibutani, T., Ito, K., Ohmi, S., Hirose, I., Morishita, K., 2005. Observation of earthquakes in Kii Peninsula under Special Project for Earthquake Disaster Mitigation in Urban Areas ~Outline of observation system and data processing~ (in Japanese with English abstract). *Disaster Prev. Res. Inst. Annu.* 48, 269–278.
- Obara, K., 2002. Nonvolcanic deep tremor associated with subduction in southwest Japan. *Science* 296, 1679–1681. <https://doi.org/10.1126/science.1070378>.
- Obara, K., Kato, A., 2016. Connecting slow earthquakes to huge earthquakes. *Science* 353, 253–257. <https://doi.org/10.1126/science.aaf1512>.
- Obara, K., Hirose, H., Yamamizu, F., Kasahara, K., 2004. Episodic slow slip events accompanied by non-volcanic tremors in southwest Japan subduction zone. *Geophys. Res. Lett.* 31, L23602. <https://doi.org/10.1029/2004GL020848>.
- Obara, K., Tanaka, S., Maeda, T., Matsuzawa, T., 2010. Depth-dependent activity of non-volcanic tremor in southwest Japan. *Geophys. Res. Lett.* 37, L13306. <https://doi.org/10.1029/2010GL043679>.
- Ohta, K., Ide, S., 2011. Precise hypocenter distribution of deep low-frequency earthquakes and its relationship to the local geometry of the subducting plate in the Nankai subduction zone, Japan. *J. Geophys. Res. Solid Earth* 116, B01308. <https://doi.org/10.1029/2010JB007857>.
- Okada, Y., Nishimura, T., Tabei, T., Matsushima, T., Hirose, H., 2022. Development of a detection method for short-term slow slip events using GNSS data and its application to the Nankai subduction zone. *Earth Planets Space* 74, 18. <https://doi.org/10.1186/s40623-022-01576-8>.
- Ökeler, A., 2021. Application of iteratively truncated singular value decomposition to computation of teleseismic receiver functions. *Pure Appl. Geophys.* 178, 2953–2967. <https://doi.org/10.1007/s00024-021-02767-2>.
- Otsubo, M., Miyakawa, A., Katayama, I., Okazaki, K., 2019. An inhomogeneous across-slab conduit controlled by intraslab stress heterogeneity in the Nankai subduction zone. *Sci. Rep.* 9. <https://doi.org/10.1038/s41598-018-38142-w>.
- Pérez-Campos, X., Kim, Y., Husker, A., Davis, P.M., Clayton, R.W., Iglesias, A., Pacheco, J.F., Singh, S.K., Manea, V.C., Gurnis, M., 2008. Horizontal subduction and truncation of the Cocos Plate beneath central Mexico. *Geophys. Res. Lett.* 35, L18303. <https://doi.org/10.1029/2008GL035127>.
- Rogers, G., Dragert, H., 2003. Episodic tremor and slip on the Cascadia subduction zone: The chatter of silent slip. *Science* 300, 1942–1943. <https://doi.org/10.1126/science.1084783>.
- Ruan, Y., Ito, Y., Sawaki, Y., 2023. Anisotropic velocity structure beneath Shikoku, Japan: insights from receiver function and shear wave splitting analyses. *J. Geophys. Res. Solid Earth* 128, e2023JB027178. <https://doi.org/10.1029/2023JB027178>.
- Saiga, A., Kato, A., Sakai, S., Iwasaki, T., Hirata, N., 2011. Crustal anisotropy structure related to lateral and down-dip variations in interplate coupling beneath the Kii Peninsula, SW Japan. *Geophys. Res. Lett.* 38, 2011GL047405. <https://doi.org/10.1029/2011GL047405>.
- Saiga, A., Kato, A., Kurashimo, E., Iidaka, T., Okubo, M., Tsumura, N., Iwasaki, T., Sakai, S., Hirata, N., 2013. Anisotropic structures of oceanic slab and mantle wedge in a deep low-frequency tremor zone beneath the Kii Peninsula, SW Japan. *J. Geophys. Res. Solid Earth* 118, 1091–1097. <https://doi.org/10.1002/jgrb.50069>.
- Sawaki, Y., Ito, Y., Ohta, K., Shibutani, T., Iwata, T., 2021. Seismological structures on bimodal distribution of deep tectonic tremor. *Geophys. Res. Lett.* 48, e2020GL092183. <https://doi.org/10.1029/2020GL092183>.
- Shelly, D.R., Beroza, G.C., Ide, S., Nakamura, S., 2006. Low-frequency earthquakes in Shikoku, Japan, and their relationship to episodic tremor and slip. *Nature* 442, 188–191. <https://doi.org/10.1038/nature04931>.
- Shelly, D.R., Beroza, G.C., Ide, S., 2007. Non-volcanic tremor and low-frequency earthquake swarms. *Nature* 446, 305–307. <https://doi.org/10.1038/nature05666>.
- Shibutani, T., Hirahara, K., 2017. 3D seismic velocity structure beneath Kii Peninsula, southwestern Japan derived from receiver function analysis and seismic tomography. In: *IAG-IASPEI Kobe, Japan pp. J08-P-12*.
- Shibutani, T., Ueno, T., Hirahara, K., 2008. Improvement in the extended-time multitaper receiver function estimation technique. *Bull. Seismol. Soc. Am.* 98, 812–816. <https://doi.org/10.1785/0120070226>.
- Shibutani, T., Hirahara, K., Ueno, T., 2009. Receiver function analyses for estimating seismic velocity discontinuity structure (in Japanese with English abstract). *Zisin (Journal Seismol. Soc. Japan. 2nd ser.)* 61, 199–207. <https://doi.org/10.4294/zisin.61.199>.
- Shina, T., Amezawa, Y., Horikawa, H., Imanishi, K., Uchide, T., 2024. Deep crustal fluids and their relation to cutoff depths of crustal earthquakes in the North Ibaraki area of northeastern Japan inferred from reflected S-waves. *Tectonophysics* 885, 230415. <https://doi.org/10.1016/j.tecto.2024.230415>.
- Shinjoe, H., Shimoda, G., Fukuoka, T., Sumii, T., 2005. Magnesian igneous enclave in the Ohmine Granitic Rocks of Kii Peninsula (in Japanese with English abstract). *Japan. Mag. Mineral. Petrol. Sci.* 34, 15–23. <https://doi.org/10.2465/gkk.34.15>.
- Shiomi, K., Park, J., 2008. Structural features of the subducting slab beneath the Kii Peninsula, central Japan: Seismic evidence of slab segmentation, dehydration, and anisotropy. *J. Geophys. Res. Solid Earth* 113, B10318. <https://doi.org/10.1029/2007JB005535>.
- Shiomi, K., Matsubara, M., Ito, Y., Obara, K., 2008. Simple relationship between seismic activity along Philippine Sea slab and geometry of oceanic Moho beneath southwest Japan. *Geophys. J. Int.* 173, 1018–1029. <https://doi.org/10.1111/j.1365-246X.2008.03786.x>.
- Shiomi, K., Takeda, T., Ueno, T., 2020. Seismological evidence of a dehydration reaction in the subducting oceanic crust beneath western Shikoku in southwest Japan. *Geophys. J. Int.* 224, 151–168. <https://doi.org/10.1093/gji/ggaa423>.
- Takemura, S., Hamada, Y., Okuda, H., Okada, Y., Okubo, K., Akuhara, T., Noda, A., Tonegawa, T., 2023. A review of shallow slow earthquakes along the Nankai Trough. *Earth Planets Space* 75, 164. <https://doi.org/10.1186/s40623-023-01920-6>.
- Tian, D., Uieda, L., Leong, W.J., Schlitzer, W., Fröhlich, Y., Grund, M., Jones, M., Toney, L., Yao, J., Magen, Y., Jing-Hui, T., Materna, K., Belem, A., Newton, T., Anant, A., Ziebarth, M., Quinn, J., Wessel, P., 2023. PyGMT: A Python interface for the Generic Mapping Tools (v0.10.0). *Zenodo*. <https://doi.org/10.5281/zenodo.8303186>.
- Uchide, T., 2020. Focal mechanisms of small earthquakes beneath the Japanese islands based on first-motion polarities picked using deep learning. *Geophys. J. Int.* 223, 1658–1671. <https://doi.org/10.1093/gji/ggaa401>.
- Uchide, T., Shiina, T., Imanishi, K., 2022. Stress map of Japan: detailed nationwide crustal stress field inferred from focal mechanism solutions of numerous microearthquakes. *J. Geophys. Res. Solid Earth* 127, e2022JB024036. <https://doi.org/10.1029/2022JB024036>.
- Ueno, T., Shibutani, T., Ito, K., 2008. Configuration of the continental Moho and Philippine Sea slab in southwest Japan derived from receiver function analysis: Relation to subcrustal earthquakes. *Bull. Seismol. Soc. Am.* 98, 2416–2427. <https://doi.org/10.1785/0120080016>.
- Umeda, K., Daijiri, U., Ogawa, Y., Kudo, T., Kakuta, C., 2003. Deep structure of the Miocene igneous complex in the Kii Peninsula, southwest Japan, inferred from wide-band magnetotelluric soundings (in Japanese with English abstract). *Bull. Volcanol. Soc. Japan* 48, 461–470. <https://doi.org/10.18940/kazan.48.6.461>.
- Umeda, K., Ogawa, Y., Asamori, K., Oikawa, T., 2006. Aqueous fluids derived from a subducting slab: Observed high ³He emanation and conductive anomaly in a non-volcanic region, Kii Peninsula southwest Japan. *J. Volcanol. Geotherm. Res.* 149, 47–61. <https://doi.org/10.1016/j.jvolgeores.2005.06.005>.
- Wang, Y., Pavlis, G.L., 2016. Generalized iterative deconvolution for receiver function estimation. *Geophys. J. Int.* 204, 1086–1099. <https://doi.org/10.1093/gji/ggv503>.
- Wessel, P., Luis, J.F., Uieda, L., Scharroo, R., Wobbe, F., Smith, W.H.F., Tian, D., 2019. The Generic Mapping Tools Version 6. *Geochemistry. Geophys. Geosyst.* 20, 5556–5564. <https://doi.org/10.1029/2019GC008515>.
- Yamauchi, M., Hirahara, K., Shibutani, T., 2003. High resolution receiver function imaging of the seismic velocity discontinuities in the crust and the uppermost mantle beneath southwest Japan. *Earth Planets Space* 55, 59–64. <https://doi.org/10.1186/BF03352463>.